HHS Public Access

Author manuscript

Cell. Author manuscript; available in PMC 2023 November 23.

Published in final edited form as:

Cell. 2022 November 23; 185(24): 4654–4673.e28. doi:10.1016/j.cell.2022.10.003.

Architecture of the outbred brown fat proteome defines regulators of metabolic physiology

Haopeng Xiao[1,2,16,*], **Luiz H. M. Bozi**[1,2,16], **Yizhi Sun**[1,2,16], **Christopher L. Riley**[1,2,16], **Vivek M. Philip**[3], **Mandy Chen**[3], **Jiaming Li**[2], **Tian Zhang**[2], **Evanna L. Mills**[1,2], **Margo P. Emont**[4], **Wenfei Sun**[5], **Anita Reddy**[1,2], **Ryan Garrity**[1], **Jiani Long**[6], **Tobias Becher**[7], **Laura Potano Vitas**[2], **Dina Laznik-Bogoslavski**[1], **Martha Ordonez**[1,2], **Xinyue Liu**[2], **Xiong Chen**[1], **Yun Wang**[1,2,8], **Weihai Liu**[1], **Nhien Tran**[1], **Yitong Liu**[1], **Yang Zhang**[9], **Aaron M. Cypess**[10], **Andrew P. White**[11], **Yuchen He**[4], **Rebecca Deng**[12], **Heiko Schöder**[12], **Joao A. Paulo**[2], **Mark P. Jedrychowski**[1,2], **Alexander S. Banks**[4], **Yu-Hua Tseng**[9], **Paul Cohen**[7], **Linus T. Tsai**[4], **Evan D. Rosen**[4], **Samuel Klein**[13], **Maria Chondronikola**[14], **Fiona E. McAllister**[15], **Nick Van Bruggen**[15], **Edward L. Huttlin**[2], **Bruce M. Spiegelman**[1,2], **Gary A. Churchill**[3], **Steven P. Gygi**[2], **Edward T. Chouchani**[1,2,17,*]

[1)]Department of Cancer Biology, Dana-Farber Cancer Institute, Boston, MA 02215, USA.

[2)]Department of Cell Biology, Harvard Medical School, Boston, MA 02115, USA.

[3)]The Jackson Laboratory, Bar Harbor, ME 04609, USA.

[4)]Division of Endocrinology, Diabetes and Metabolism, Beth Israel Deaconess Medical Center and Harvard Medical School, Boston, MA 02215, USA.

[5)]School of Engineering, Stanford University, Stanford, CA 94305, USA.

[6)]College of Computing, Georgia Institute of Technology, Atlanta, GA 30332, USA.

[7)]Laboratory of Molecular Metabolism, The Rockefeller University, New York, NY 10065, USA.

[*]Correspondence: haopeng_xiao@dfci.harvard.edu (H.X.), edwardt_chouchani@dfci.harvard.edu (E.T.C.).

Author Contributions

E. T. C. and H. X. conceived of and directed the study, and wrote the manuscript. H. X. performed outbred animal experiments, mass spectrometry, bioinformatics, and assisted in biological validations. L. H. M. B, Y. S., and C. L. R. design and conducted biological validations (ATP1A2, L. H. M. B.; SFXN5, Y. S.; LETMD1, C. L. R. and Y. S.). V. M. P., M. Chen, and G. A. C. performed QTL mapping and strain selection analysis. J. Li, T. Z., J. Long, X. L., J. A. P., M. P. J., and E. L. H. assisted in mass spectrometry and bioinformatics. E. L. M., A. R., R. G., D. L., M. O., Y. W., X. C., W. L., N. T., Y. H., L. P. V., and Y. L. assisted in cellular and animal experiments. T. B. and P. C. assisted in human phenotypic variation analysis. M. P. E. and W. S. assistant in cell population deconvolution. R. D. and H. S. collected human BAT activity and phenotypic data. Y. Z., A. M. C., A. P. W., and Y. T. collected human BAT and SAT microarray data. S. K. and M. Chondronikola collected human BAT RNA-seq and phenotype data. M. P. E., L. T. T., and E. D. R. collected human SAT RNA-seq and phenotype data. H. X. and J. Li built the website. A. S. B., Y. T., P. C., L. T. T., E. D. R., S. K., M. Chondronikola, F. E. M., N. V. B., E. L. H., B. M. S., G. A. C., S. P. G., and E. T. C. oversaw the experiments and data analyses. All authors edited the manuscript.

Declaration of Interests

F.E.M and N.V.B and are currently employees of Calico Life Sciences LLC. T.B. is currently an employee of Roche Diagnostics. E.T.C is a founder, equity holder, and consultant for Matchpoint Therapeutics and Aevum Therapeutics. B.M.S is a founder, equity holder, and consultant for Aevum Therapeutics.

[8)]Guanghua School of Stomatology, Sun Yat-sen University, Guangzhou, Guangdong 510275, China.

[9)]Section on Integrative Physiology and Metabolism, Joslin Diabetes Center, Harvard Medical School, Boston, MA 02215, USA.

[10)]Diabetes, Endocrinology, and Obesity Branch, National Institute of Diabetes and Digestive and Kidney Diseases, National Institutes of Health, Bethesda, MD 20892, USA.

[11)]Department of Orthopedic Surgery, Beth Israel Deaconess Medical Center and Harvard Medical School, Boston, MA 02215, USA.

[12)]Department of Radiology, Memorial Sloan Kettering Cancer Center, New York, NY 10065, USA.

[13)]Center for Human Nutrition, Washington University School of Medicine, St. Louis, MO 63110, USA.

[14)]Department of Nutrition, UC Davis, Davis, CA 95616, USA.

[15)]Calico Life Sciences LLC, South San Francisco, CA 94080, USA.

[16)]These authors contributed equally.

[17)]Lead contact

Abstract

Brown adipose tissue (BAT) regulates metabolic physiology. However, nearly all mechanistic studies of BAT protein function occur in a single inbred mouse strain, which has limited understanding of generalizable mechanisms of BAT regulation over metabolism. Here we perform deep quantitative proteomics of BAT across a cohort of 163 genetically defined Diversity Outbred mice, a model that parallels the genetic and phenotypic variation found in humans. We leverage this diversity to define the functional architecture of the outbred BAT proteome, comprising 10,479 proteins. We assign co-operative functions to 2,578 proteins, enabling systematic discovery of regulators of BAT. We also identify 638 proteins that correlate with protection from, or sensitivity to, at least one parameter of metabolic disease. We use these findings to uncover SFXN5, LETMD1, and ATP1A2 as modulators of BAT thermogenesis or adiposity, and provide OPABAT as a resource for understanding conserved mechanisms of BAT regulation over metabolic physiology.

In Brief

A mass spectrometry and network analysis approach leverages the natural genetic, proteomic, and phenotypic diversity found in the brown adipose tissue of outbred populations to annotate thousands of regulatory proteins of metabolic physiology.

Graphical Abstract

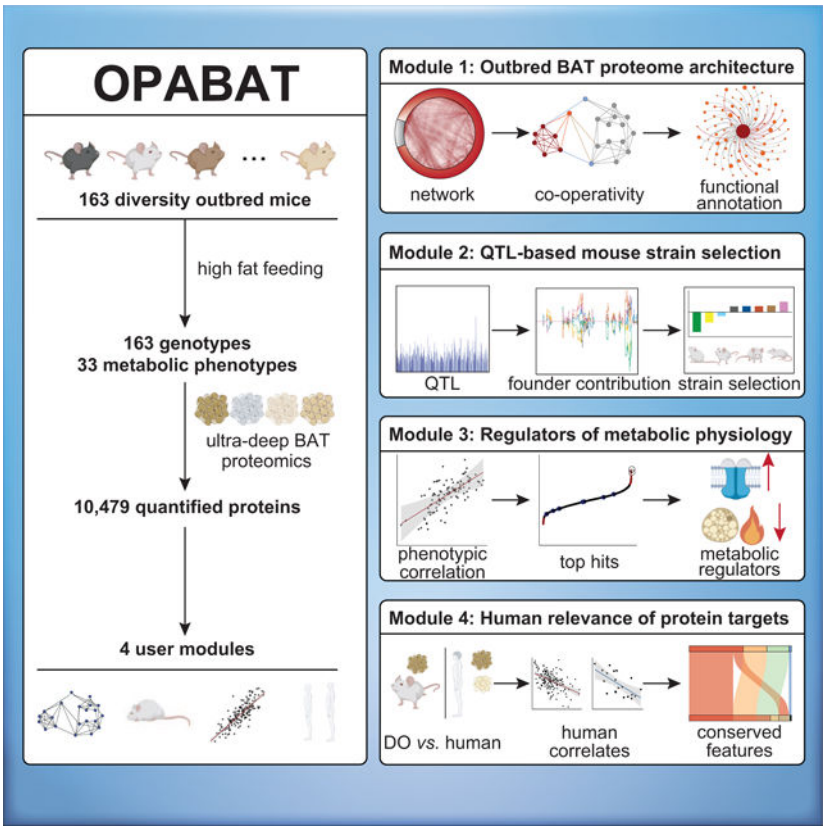

Introduction

Metabolic diseases are among the most common human pathologies and exhibit variable penetrance in the population. Genetic variation is a major factor determining sensitivity to, or protection from, metabolic diseases (Barroso and McCarthy, 2019; Speliotes et al., 2010). Genetic differences lead to altered protein abundance or function, which affects sensitivity to environmental drivers of pathogenesis. Brown adipose tissue (BAT) and beige fat harbor distinct proteomes that can coordinate rapid catabolism of energy sources in futile cycles. For this reason, BAT thermogenic proteins have been widely studied for their capacity to regulate energy expenditure, systemic metabolism, and metabolic disease (Chouchani et al., 2019; Muller et al., 2016; Wang and Seale, 2016). BAT catabolic activity in human is highly variable and exhibits strong negative correlations with metabolic disease parameters (Becher et al., 2021). As such, understanding the molecular basis governing the divergence of BAT function across a genetically diverse population could yield insights into common regulators of metabolic disease.

In human populations, determining the molecular basis for differences in BAT function and metabolic disease sensitivity is limited by confounding lifestyle and environmental covariates. Therefore, characterization of BAT function and physiology has relied largely on the use of murine models. However, most studies characterizing BAT molecular biology and physiology over the last half century have used a single strain, C57BL/6. Although convenient, the substantial heterogeneity of BAT function and metabolic disease sensitivity

exhibited by outbred populations is completely lacking in C57BL/6. Moreover, lack of biological variation in an isogenic cohort hinders discovery of orphan protein functions through analysis of co-variance with proteins of known function (Kustatscher et al., 2022a). Currently, most BAT proteins are not unambiguously annotated to a biological function or pathway (Ashburner et al., 2000; Gene Ontology, 2021; Giurgiu et al., 2019; Kanehisa et al., 2021; Ruepp et al., 2010; UniProt, 2021). It stands to reason that detailed molecular and functional analysis of BAT in defined outbred populations would improve the understanding and translational potential of this tissue.

Recent advances in quantitative mass spectrometry have enabled comprehensive proteomics in genetically diverse samples (Chick et al., 2016; Keele et al., 2021). Here we perform deep quantitative multiplexed proteomics of BAT across 163 fully genotyped Diversity Outbred (DO) mice (Figure 1A), a population model that parallels the genetic and phenotypic variation found in humans (Chick et al., 2016; Churchill et al., 2012; Saul et al., 2019). This dataset presents the deepest quantitative proteome landscape in BAT and captures over 100-fold deeper coverage of strain diversity of the BAT proteome than is currently known, in a phenotyped population. We leverage this dataset to define the functional Outbred Proteome Architecture of BAT (OPABAT), providing four “modules” for the research community:

Module 1: Proteome architecture to annotate biological function of BAT proteins.

We develop a systematic co-expression network to define the architecture of the outbred BAT proteome. We assign co-operative functions to 2,578 proteins with 780 established protein networks, in order to systematically annotate regulators of BAT function. We use this approach to show that two understudied proteins, LETM1 domain-containing protein 1 (LETMD1) and sideroflexin-5 (SFXN5), are key modulators of the widely studied thermogenic protein uncoupling protein 1 (UCP1).

Module 2: Strain selection for modeling metabolic phenotypes.

We perform Quantitative Trait Locus (QTL) mapping for 8,923 proteins and 33 metabolic phenotypes, and quantify founder strain allelic contributions to phenotypes. This analysis scores 42 commercially available mouse strains that are most likely to exhibit specific metabolic phenotypes or BAT protein expression levels, providing a resource for rational selection of mouse strains.

Module 3: Discovery of BAT proteins that correlate with metabolic physiology and disease.

We identify 638 proteins that underlie protection from, or sensitivity to, at least one of 19 different metabolic disease parameters. Some of these proteins already have well-characterized roles in BAT biology and metabolic disease, while most do not. These assignments provide a repertoire of targets for mechanistic investigation. From this basis, we discover that the Na^+/K^+-ATPase α2 subunit is an in inhibitor of brown adipocyte energy expenditure, through antagonism of calcium influx-dependent activation of thermogenic effectors.

Module 4: Mapping BAT protein targets relevant to outbred human physiology and disease.

We determine the relevance of OPABAT protein-phenotype correlates in human metabolic physiology by mapping tissue enrichment, phenotypic correlations, and disease network involvement in human cohorts. This creates a roadmap to evaluate the translational value of OPABAT protein targets in human.

Together, we provide OPABAT (wren.hms.harvard.edu/opabat/) as a resource for understanding conserved mechanisms of BAT regulation over metabolic physiology.

Results and discussion

Defining the genotypes, phenotypes, and BAT proteomes of a DO cohort

Our discovery cohort comprised 163 fully-genotyped female DO mice. The genetic diversity of the DO cohort is in great excess of standard isogenic mouse strains, and parallels the human population (Figure 1B and S1A) (Bergstrom et al., 2020; Frazer et al., 2007; Saul et al., 2019; Simon et al., 2013; Yang et al., 2011). This cohort was analyzed for major metabolic phenotyping parameters associated with obesity and BAT function, under baseline conditions and during 8-weeks of high fat diet (HFD) feeding at thermoneutrality (TN) (Figure 1C and Methods). Interscapular BAT from all mice were isolated for mass-spectrometry (MS)-based proteomics analysis. Mice possess numerous adipose depots that contain thermogenic adipocytes, both brown and beige. In mice housed at thermoneutrality, interscapular BAT represents the most robust and homogeneous source of thermogenic adipocytes, which closely recapitulate the thermogenic function of the corresponding human cells (de Jong et al., 2019; Roh et al., 2018; Shinoda et al., 2015). For this reason, we selected interscapular BAT for proteomic characterization.

Outbred proteomics has been a major technical challenge due to technical variability inherent to large sample sizes and peptide sequence heterogeneity. To address this, we used sample multiplexing afforded by TMTpro 16-plex reagents and the current most advanced instrumentation for protein quantification (Figure 1D&S1B). We performed *in silico* whole proteome digestion of the eight founder strains from which DO mice are generated (Churchill et al., 2012), to obtain a database containing peptides shared by all genetic founders for peptide filtering (Figure S1C). To test the robustness of this strategy, we randomly selected thirteen BAT proteomes from the DO cohort to measure in triplicates, within the same TMT plex and across 12 separate TMT plexes. We observed no sample clustering attributable to TMT batch (Figure S1D&E), and low technical variability (Figure S1F&G). These results demonstrate that the above approach allows for accurate quantitation of outbred BAT proteomes.

Using the workflow described above, we quantified 10,479 proteins with high confidence in the entire DO cohort (Table S1), of which ~70% were quantified in every mouse (Figure S1H). Every TMT plex quantified an average of ~9,000 proteins in BAT (Figure S1I-K). This proteome coverage in mouse BAT is 34–74% higher than those in previous reports (Figure 1E) (Hu et al., 2020; Huttlin et al., 2010; Kazak et al., 2015; Kazak et al., 2017b; Kazak et al., 2019; Li et al., 2020a; Williams et al., 2018; Yu et al., 2020; Zeng et al., 2019),

with ~10 fold more low-abundance proteins quantified (Figure 1F&S1L). Unlike previous proteomic efforts, here we quantified proteins in an outbred cohort, which manifests genetic perturbations that generate protein expression variability consistent within the bounds of a natural population. The substantial variation in protein abundance within the DO cohort is much less pronounced in isogenic cohorts (Figure S1M), which allowed us to derive co-variations to systematically define co-regulatory protein interactions and construct OPABAT.

Module 1: Co-expression network analysis to define OPABAT

While many BAT proteins have been extensively studied (Chouchani et al., 2019; Muller et al., 2016; Wang and Seale, 2016), the large majority of the 10,479 proteins quantified in OPABAT were not unambiguously annotated to a specific complex or biological function (Ashburner et al., 2000; Gene Ontology, 2021; Giurgiu et al., 2019; Kanehisa et al., 2021; Ruepp et al., 2010; UniProt, 2021) (Figure S2A & Table S1). Functional proteomics has emerged as a tool to annotate understudied proteins through assessing protein co-regulation (Kustatscher et al., 2022a, b). This principle relies on assessing correlation in abundance of proteins across heterogeneous populations, and has been applied for robust identification of coordinated protein functions, and protein complexes and pathways (Bludau, 2021; Kustatscher et al., 2019; Romanov et al., 2019; Stalder et al., 2020). Here we leveraged the deep OPABAT proteome to systematically annotate protein functions based on correlated expression. Like previous studies (Antonicka et al., 2020; Li et al., 2019; Nusinow et al., 2020), we calculated Pearson correlation between the expression profiles of every possible pair of proteins as a measurement of protein-protein association (Figure 2A). These associations were then filtered to < 5% false discovery rate (FDR) (Strimmer, 2008a, b), resulting in a network containing 160,364 significant protein-protein correlations (termed “edges”, Table S2).

We first annotated this architecture by investigating mechanisms that might be responsible for significant correlations (Figure 2B). We superimposed our network onto Bioplex (Huttlin et al., 2021) and CORUM (Giurgiu et al., 2019), which contain high-confidence protein physical interactions and complexes (Figure 2B, Table S2). A total of 10,773 (6.7%) edges in the OPABAT network were explained by known physical interactions, which fully recapitulated 102 CORUM complexes (Figure S2B). Examples of fully and partially recapitulated complexes are displayed in Figure 2C & Figure S2C. Many of the partial networks were attributable to known transient or tissue-specific protein complexes that appear not to recapitulate in BAT (Chen et al., 2001; Staals et al., 2010). To enable more extensive investigation, we also compiled physical interactions in BioGRID (Oughtred et al., 2019), STRING (Szklarczyk et al., 2017), and MINT (Calderone et al., 2020). Overall, 17,499 (10.9%) edges were explained by known physical interactions. In addition, we investigated edges that could be explained by concerted activity in a common biological process (Ashburner et al., 2000; Gene Ontology, 2021; Jassal et al., 2020; Kanehisa et al., 2021; Thul et al., 2017), which additionally annotated 49,205 edges. Most physical interactions (79%) were also identified in coordinated pathways (Figure S2D), including metabolic pathways such as the TCA cycle (Figure 2D). Overall, 41.6 % of the co-operative edges in OPABAT were annotated based on literature evidence (Figure 2B, Table S2). This

demonstrated that co-operative network analysis of outbred proteomes produces a robust architecture based on shared biological activities of proteins.

OPABAT systematically annotates biological function of BAT proteins

In addition to reconstructing hundreds of established protein networks, we also identified 93,660 correlations that were previously undescribed. We next systematically annotated protein biological functions based on protein co-operativity. The existence of co-operative protein interactions with known complexes or pathways was determined by scoring the enrichment of co-operative edges (Figure 2E & Methods) (Huttlin et al., 2020). In total, we identified 515 out of ~3,500 CORUM core complexes that harbor 1,736 co-operative proteins in OPABAT (Figure 2F). Prominent examples include co-operative network members with the proteasome subunits and the mTORC1 complex (Figure 2G&S2E). To validate our results, we queried these interactions for experimental evidence that could support physical interactions between the protein and the complex (Huttlin et al., 2021), and annotated 923 co-operative events. The total number of co-operative proteins vary greatly across different complexes (Figure 2F, Table S3). In parallel, we also identified 2,345 proteins associated with 265 established KEGG pathways (Figure S2F, Table S3).

Systematic determination of 2,578 proteins (24.6% of OPABAT proteome coverage) exhibiting co-operativity with established protein networks provides a clear rationale for illuminating biological functions for these targets. We therefore next investigated whether newfound co-operative proteins could be used as a basis to identify regulators of BAT thermogenic function. To do so, we examined co-operative partners with proteins that have well-established roles in thermogenesis (Figure 2H&S2G). Among the most widely studied thermogenic proteins is UCP1, which is exclusively expressed in brown and beige fat (Ikeda et al., 2018). UCP1 is a major effector of thermogenic respiration and thought to contribute to the protective activity of BAT against metabolic disease (Chouchani et al., 2019). UCP1 abundance and activity are subject to strict upstream regulation, but the proteins that maintain UCP1 abundance and activity remain poorly characterized. Interestingly, our network analysis revealed 84 proteins that exhibit significant co-operativity with UCP1, of which only 14 have previously been associated with UCP1 (Ashburner et al., 2000; Kanehisa et al., 2021) (Figure 2I, Table S2). Among the strongest co-operative interactions with UCP1 were two largely uncharacterized proteins: LETMD1 and SFXN5 (Figure 2I).

LETMD1 is a regulator of UCP1 abundance and BAT thermogenesis

LETMD1 is highly co-operative with UCP1 in outbred BAT (Figure 3A). On this basis, we explored the role of LETMD1 in UCP1 function and BAT activity. We first confirmed the existence and high relative abundance of LETMD1 isoform 1, which drove the correlation with UCP1 (Figure S3A-C). We then examined the tissue expression of LETMD1 and observed that like UCP1, it is selectively expressed in BAT and beige fat (Figure 3B). Moreover, like UCP1, LETMD1 expression was cold-inducible in BAT and it was localized to the mitochondrial inner membrane in brown adipocytes (Figure 3C-F). Based on this, we generated LETMD1 knockout mice to explore possible regulation of UCP1 by LETMD1 (Figure S3D). Remarkably, loss of LETMD1 resulted in an abrogation of UCP1 protein in BAT and whitening of BAT (Figure 3G&H & Figure S3E&F). Moreover, depletion

of LETMD1 in differentiated brown adipocytes significantly compromised thermogenic capacity (Figure 3I), which coincided with the highly selective loss of UCP1 protein (Figure 3J&K), independent of effects on expression of other thermogenic factors or mitochondrial respiratory chain complexes (Figure S3G-K). Indeed, mice lacking LETMD1 also exhibited severely compromised capacity for BAT-dependent adaptive thermogenesis (Figure 3L-N). These findings agree with reports published when this study was under review, which also illustrated a critical role for mitochondrial LETMD1 in regulating BAT thermogenesis (Choi et al., 2021; Snyder et al., 2021). Together, our data identify LETMD1 as a regulator of UCP1 abundance and adaptive thermogenesis in BAT, and demonstrate how co-operative network analysis of the outbred BAT proteome can be used to identify biological roles for poorly characterized proteins.

SFXN5 is a regulator of UCP1-dependent thermogenesis by supporting mitochondrial glycerol-3-phosphate utilization

SFXN5 is a poorly understood mitochondrial membrane protein with no known role in BAT (Tifoun et al., 2021). In OPABAT, SFXN5 exhibited the highest proteome-wide co-operativity with UCP1 (Figure 3O) while SFXN1–4 were not significantly correlated with UCP1 (Table S2). Like UCP1 and LETMD1, SFXN5 was highly expressed in BAT (Figure S3L) (Geiger et al., 2013), and its transcript expression was highly cold-inducible (Figure S3M) (Roh et al., 2018). Moreover, we found that SFXN5 localization was restricted to the inner mitochondrial membrane, where UCP1 is located (Figure 3F & S3N&O). These data led us to hypothesize that SFXN5 regulates UCP1-dependent thermogenesis in BAT. To test this, we depleted SFXN5 in differentiated primary brown adipocytes, which led to significantly compromised thermogenic capacity without affecting UCP1 abundance (Figure 3P-R). Knockdown of SFXN5 in mouse BAT attenuated whole body thermogenic responses upon exposure to cold (Figure 3S&T & S3P). Since SFXN5 is a mitochondrial protein that inhibited thermogenic respiration without affecting UCP1 protein levels, we examined whether SFXN5 regulates mitochondrial metabolic processes crucial to support UCP1-dependent thermogenesis. We applied a rapid mitochondria immunopurification method (Chen et al., 2016) (Figure S3Q&R) in wildtype and $SFXN5^{KD}$ differentiated primary brown adipocytes following adrenergic stimulation to identify mitochondrial metabolic processes that rely on SFXN5 (Figure 3U). This analysis determined that glycerol-3-phosphate (G3P) levels were significantly depleted following knockdown of SFXN5 (Figure 3V). This observation agreed with our co-operative network analysis that additionally defined SFXN5 as a novel co-operative protein of the glycerophospholipid metabolism pathway (Figure 2E & Figure 3W, Table S3), through which G3P is metabolized. G3P is known to support UCP1-mediated thermogenic respiration (Shabalina et al., 2013; Shabalina et al., 2014), and our data suggested that SFXN5 was involved in this process. To examine this further, we measured substrate utilization capacity of isolated mitochondria from differentiated primary brown adipocytes and found that depletion of SFXN5 led to lowered capacity of mitochondria to utilize G3P, while having no significant effect on pyruvate linked respiration (Figure 3X & S3S&T). Together, our data suggest that SFXN5 regulates UCP1-dependent thermogenic respiration through supporting mitochondrial metabolic utilization of G3P. This validation provides another demonstration of how OPABAT can be used to generate testable hypotheses to identify biological roles for orphan proteins.

Module 2: Mapping phenotypic variation in the DO cohort

We quantified 33 major metabolic parameters associated with obesity and BAT function, under baseline conditions and during 8 weeks of HFD feeding (Figure 4A and S4A, Table S4). We found that the DO cohort exhibited significant phenotypic heterogeneity for many of the major physiological parameters associated with metabolic disease (Figure 4A). A notable example was found in the case of the adiposity response to HFD, whereby some mice became severely obese after HFD intervention, while others exhibited significant resistance to obesity (Figure 4A and Figure S4A). This variability greatly exceeds that observed in C57BL/6J mice of similar age groups under HFD (Figure S4B) (Bogue et al., 2020). Interestingly, across the cohort, certain phenotypic parameters correlated more strongly than others with each other (Figure S4C). We evaluated the extent to which the phenotypic variation in OPABAT reflects that found in human populations. We examined phenotypic data gathered from a cohort of 1,281 non-smoking patients (male=223, female=1,058) with confirmed presence of BAT and without stage-4 cancer or other severe metabolic disease (Becher et al., 2021). We found that both male and female humans exhibited a similar degree of variation in BAT activity and most metabolic phenotypes (Figure S4D). Moreover, phenotypic variation in OPABAT parallels those shown in human populations (Figure S4E), demonstrating that the DO model harbors sufficient variation to derive co-variation for analysis of molecular drivers of phenotypic outputs.

OPABAT informs mouse strain selection

By combining genetic, proteomic, and phenotypic layers of OPABAT, we generated a molecular basis for phenotype diversity across outbred mice. We performed Quantitative Trait Locus (QTL) mapping (Rockman and Kruglyak, 2006) for each of the 33 metabolic phenotypes (Figure 4B&C, Table S4). Through determining founder strain allelic contributions to 29 QTLs with logarithm of the odds (LOD) > 6, we generated a resource to guide selection across 168 commercially available collaborative cross (CC) and founder mouse strains to study specific BAT-dependent phenotypic outputs (Table S4). Mapping was performed by classifying mouse haplotypes into one of eight founder homozygous allelic states based on their genotype probabilities at a given QTL (Methods). For example, we scored many strains across a spectrum of resting energy expenditure (VO_2 cold/day; Figure 4D-F). We also investigated strains that are most likely to exhibit predisposition or resistance to obesity (Figure 4G). We found that NZO/HlLtJ (known as the New Zealand Obese) founder allelic effects contributed the most positively to predisposition to obesity, whereas 129S1/SvImJ was the strongest negative contributor (Figure 4H&I). CC001/UncJ, CC005/TauUncJ, CC009/UncJ, CC025/GeniUncJ, CC043/GeniUncJ, and CC068/TauUncJ strains are homozygous for the NZO/HlLtJ allele at this location and along with the NZO/HlLtJ founder are the top candidates for obesity predisposition models (Figure 4I).

We extended this analysis to determine mouse strains that could express specific proteins of interest in BAT. To do so, we mapped BAT protein QTLs (pQTLs), identifying 2,046 pQTLs at a genome-wide significance level of $p< 0.05$ (1390 local vs. 656 distant, Figure S4F&G, Table S4). For instance, distant pQTLs for UCP1 and LETMD1 were mapped to the 89.47 Mb position on chromosome 11 (Figure S4H). On this basis, we determined founder strain allelic effects on UCP1 expression (Figure 4J-L). NZO/HlLtJ founder allelic

effects contributed the most negatively to the expression of UCP1 (Figure 4K&L). The CC strains that are homozygous at this allele are CC003/UncJ, CC005/TauUncJ, CC011/UncJ, CC042/GeniUncJ, and CC068/TauUncJ (Figure 4L). These strains are also the top candidates to express low levels of LETMD1 in BAT (Figure S4I&J). Overall, we determine 42 commercially available strains that are most likely to exhibit specific metabolic phenotypes or protein expression levels.

Module 3: BAT protein determinants of metabolic disease in outbred mice

We next leveraged OPABAT to identify protein regulators of metabolic disease. We systematically determined correlations between protein expression and phenotypic data (Figure S5A), discovering several hundreds of proteins that significantly correlated with at least one phenotypic parameter (Figure 5A, Table S5). While some proteins shared correlation with multiple phenotypic parameters, many are unique to each parameter (Figure 5B). These findings suggest that distinct protein pathways could regulate specific features of BAT function, for example differentiating capacity for BAT to regulate response to cold exposure versus resistance to adiposity.

Our analysis identified several protein-physiological correlates for proteins known to play roles in BAT function, obesity, and metabolic disease (Figure 5C-K). For instance, two proteins exhibiting the strongest correlations with adiposity under HFD were leptin and NPR3. Leptin is a widely studied hormone that regulates food intake and body weight (Izquierdo et al., 2019; Zhang et al., 1994). Obese subjects exhibit high circulating levels of leptin and leptin resistance (Izquierdo et al., 2019). Indeed, we found that leptin in BAT is positively correlated with body weight, fat mass, and % body fat in the DO population (Figure 5C,D,F&H). Another top protein correlate, NPR3, is the clearance receptor of natriuretic peptides (NPs). NPs stimulate lipolysis in adipocytes and promote thermogenesis in brown and beige fat (Bordicchia et al., 2012). In BAT, NPR3 antagonizes NP signaling through NPR1 to suppress thermogenesis. Indeed, mice with adipose tissue-specific knockout of NPR3 exhibit increased energy expenditure and are resistant to HFD-induced obesity (Wu et al., 2017). Based on our findings, BAT NPR3 expression is a positive driver of adiposity in outbred populations (Figure 5C,D,F&I).

In inbred mice, the abundance of BAT thermogenic effector and regulator proteins are widely used to estimate thermogenic adipocyte activity and BAT-driven protection against metabolic disease (Chouchani et al., 2019; Ikeda et al., 2017; Kazak et al., 2015; Lodhi et al., 2012; Rahbani et al., 2021; Rajakumari et al., 2013; Sun et al., 2021). Remarkably, we found that, in outbred populations, the abundance of most of these factors did not correlate with any metabolic disease parameters (Figure 5C-G & 5K&L). Contrary to prevailing views, elevated abundance of these proteins appears to not be sufficient to elicit protection against metabolic disease parameters by BAT. Instead, our findings suggest that, at the level of protein expression, physiological BAT output is dictated by other components of the BAT proteomic architecture, which perhaps should be prioritized for leveraging the therapeutic activity of this tissue. Among the most prominent examples was ATP1A2, ATPase Na^+/K^+ transporting subunit α2 (Figure 5J). Abundance of ATP1A2 in BAT was the strongest positive correlating factor with % body fat increase under HFD in the DO cohort.

This result was confirmed using an orthogonal machine learning approach based on the Lasso method (Figure S5B-D, Methods). Interestingly, ATP1A2 abundance also exhibited moderate negative correlations with VO_2, VCO_2, and EE (Figure S5E), further suggesting an antagonistic role for ATP1A2 in BAT thermogenesis and BAT-mediated protection from obesity. On this basis, we performed mechanistic characterization of ATP1A2 in relation to BAT thermogenesis and energy expenditure, described in the section below.

Finally, we examined the contribution of cell population heterogeneity in driving phenotypic outputs. We performed digital cytometry of our proteomics data using a well-established algorithm (Newman et al., 2019) to deconvolute cell populations in BAT (Figure S5F-H, Methods). We found that brown adipocyte cell content across the DO cohort was negatively correlated with fat mass, body weight, and % body fat (Figure S5I-K), which highlights a major metabolic contribution of brown adipocyte to whole-body energy expenditure.

ATP1A2 inhibits BAT energy expenditure

The Na^+/K^+ transporting ATPase consists of α, β, and γ subunits. The α subunit composition is derived from either ATP1A1 or ATP1A2, and ATP1A2 expression is tissue-specific (Uhlen et al., 2015). In cardiomyocytes, increased abundance of ATP1A2 leads to hyperpolarization of the plasma membrane potential (Doganli et al., 2012), while ATP1A2 abundance correlates negatively with Ca^{2+} influx in cultured primary astrocytes (Golovina et al., 2003). Depolarization of the plasma membrane is crucial for Ca^{2+} import by voltage-dependent calcium channels (VDCC), which is an upstream response to adrenoreceptor agonism. Ca^{2+} influx is known to trigger a cAMP-mediated pathway, activating lipolysis and thermogenesis in brown adipocytes (Chen et al., 2017). Based on a role for rapid Ca^{2+} influx in regulating thermogenesis, we hypothesized that elevated abundance of ATP1A2 could inhibit brown adipocyte energy expenditure, through antagonism of calcium influx-dependent activation of thermogenic effectors (Figure 6A).

To test this model, we first examined the effects of genetic manipulation of ATP1A2 abundance in mouse primary brown adipocytes (Figure 6B). Remarkably, overexpression of ATP1A2 was sufficient to significantly blunt Ca^{2+} influx into brown adipocytes upon adrenergic stimulation (Figure 6C). Conversely, siRNA depletion of ATP1A2 sensitized adipocytes to NE-dependent Ca^{2+} influx (Figure 6D). We next examined downstream thermogenic signaling. Using quantitative phosphoproteomics, we found that overexpression of ATP1A2 significantly decreased phosphorylation of PKA targets following adrenergic stimulation (Figure 6E). Moreover, NE-dependent elevation of lipolysis and thermogenic respiration were significantly inhibited through elevation of ATP1A2 (Figure 6F&G). Taken together, our data demonstrate that elevated abundance of ATP1A2 antagonizes the thermogenic adrenoreceptor-mediated response in brown adipocytes. We next overexpressed ATP1A2 in mature BAT of 8-week-old adiponectin-Cre (cyclic recombinase) C57BL/6J mice via local delivery to BAT of adeno-associated virus (AAV) with Cre-driven expression of ATP1A2, and monitored the obesogenic response of control and ATP1A2-overexpressing mice under 8-week HFD and thermoneutral conditions (Figure 6H-J & S6A). We found that elevation of ATP1A2 in BAT led to significantly higher % body fat increase in $ATP1A2^{OE}$ mice compared to GFP^{OE} control following HFD (Figure 6K), absent differences in food

intake or lean mass (Figure 6L&M). The difference in % body fat increase was more striking than other measurements of adiposity (Figure 6K & S6B&C). Analysis of specific fat depots determined that this difference was attributable to a relatively large increase in epididymal fat mass of the ATP1A2^{OE} mice (Figure 6N&S6D-H). Next, we depleted ATP1A2 in the BAT of C57BL/6J mice (Figure 6O), which decreased lipid content and attenuated whitening of BAT under HFD and thermoneutrality (Figure 6P-R). This was associated with lower % body fat and SAT mass, among measurements of adiposity (Figure S6I-Q), absent differences in food intake or lean mass (Figure S6R&S). On molecular level, knockdown of ATP1A2 in BAT led to elevation in expression of key effectors in fatty acid oxidation and oxidative phosphorylation, downstream of PKA signaling in thermogenesis (Figure S6T-V). Together, these results demonstrate that manipulation of ATP1A2 expression in BAT is sufficient to dynamically regulate BAT function and adiposity in an obesogenic environment. These data exemplify how OPABAT can be used to systematically identify novel regulators of BAT-mediated protection from metabolic disease.

Module 4: OPABAT protein-phenotype correlators are recapitulated in human

We next explored the extent to which OPABAT protein-phenotype correlators are relevant in human populations. First, we examined microarray data to compare transcript abundance in deep neck BAT and superficial/subcutaneous SAT from 10 human patients (Table S6). We found that the transcripts of OPABAT phenotype-correlated proteins were more highly expressed in human BAT than SAT (Figure 7A). Next, we examined whether the protein-phenotype correlations observed in OPABAT recapitulate in human. To do so, we collected phenotypic and supraclavicular adipose tissue (SCVAT) transcript data from a de-identified human cohort of 20 individuals (Table S6). SCVAT is the major site of BAT in human (Nedergaard et al., 2007). Thirty-nine quantitative phenotypic parameters were measured in this cohort under thermoneutral or room temperature conditions (Figure 7B), in parallel with RNA-seq analysis of SCVAT biopsies. For each parameter that we measured in OPABAT, we analyzed how many of the mouse protein correlators are recapitulated as human transcript-phenotype correlators (Figure 7C&S7A, Table S6). Between 8%−39% protein correlators were recapitulated for human adiposity phenotypes (Figure 7D&E). For instance, 174 OPABAT body weight correlators were recapitulated as human BMI correlators (Figure 7F). These data demonstrated that despite potential discordance between protein and mRNA expression, a large portion of OPABAT phenotypic correlators were recapitulated in human populations. We next investigated human SAT, which exhibits capacity for inducible thermogenesis (Figure 7G). We analyzed the correlations between phenotypes and transcripts in the SAT of a human cohort of 43 individuals (Emont et al., 2022). Between 22% to 30% of the protein correlators of adiposity in OPABAT were recapitulated as phenotype-transcript correlators in human SAT (Figure 7H-I&S7B), and body mass index (BMI) was the human phenotype that enriched most of the OPABAT correlators (Figure 7J). Together, these data strongly demonstrate that protein-phenotype correlators identified in DO mice are recapitulated in human populations.

Lastly, we systematically explored the human disease involvement of OPABAT protein correlators of metabolic phenotypes. We mapped these targets onto DisGeNET (Pinero et al., 2020; Pinero et al., 2021), a comprehensive collection of established human disease-linked

genes (Figures S7C). We identified highly significant mapping of OPABAT correlators onto human disease networks (Figures S7C-E and Table S7), such as obesity, diabetes, and metabolic disease-linked liver pathology (Figure S7F-J). Many of these proteins were recapitulated as phenotype correlators in human (Figure S7F-J, Table S6). Although BAT metabolism has been linked to a broad spectrum of diseases (Becher et al., 2021; Cypess and Kahn, 2010), the molecular targets underlying these links are not well understood. Our analysis here reveals proteins in BAT that could be prioritized for analysis of relevance to human metabolic disease through modulation of BAT function.

Conclusions

OPABAT represents the deepest quantitative landscape of the mouse outbred BAT proteome. We leverage the heterogeneity of this model to perform co-variation analysis to investigate genetic and proteomic determinants of BAT function and metabolic physiology. We use these findings to uncover SFXN5, LETMD1, and ATP1A2 as modulators of BAT thermogenesis and adiposity. Together, this work demonstrates how deep outbred proteomics can aid in discovery of biological activities of understudied proteins. We envision that the four modules in OPABAT will serve as a basis to stimulate hypothesis-driven studies to investigate translationally-relevant BAT proteins in metabolic disease.

Limitations of the study

The OPABAT resource has several limitations. The discovery cohort is composed of female mice due to difficulty in group housing and metabolic assessments of male outbred mice (Logan et al., 2013; Recla et al., 2014). Although we show that male and female populations harbor a similar degree of phenotypic variation for co-variation analysis, and the biological targets that we validated, LETMD1, SFXN5, and ATP1A2, are generalizable in male mice, we are unable to attain a systematic generalizability assessment between sexes for all the protein targets that we identified. In addition, the outbred cohorts are necessarily based on each individual being distinct. As such, we are unable to perform invasive protein measurements in a pre/post intervention study design for this work, which may additionally reveal causal relationships between protein abundance and phenotypes.

STAR METHODS

RESOURCE AVAILABILITY

Lead contact—Further information and requests for resources and reagents should be directed to and will be fulfilled by the Lead contact, Edward Chouchani (edwardt_chouchani@dfci.harvard.edu), upon reasonable request.

Materials availability—No new unique reagents were generated in this study. Other materials can be requested from the Lead contact.

Data and code availability—All OPABAT raw MS files are deposited to the ProteomeXchange Consortium via the PRIDE (Perez-Riverol et al., 2019) partner repository with the dataset identifier PXD036947. All processed data are available for download at https://wren.hms.harvard.edu/opabat/.

Source codes for the OPABAT site are deposited in Github (https://github.com/Angrycodeboy/OPABAT).

Any additional information required to reanalyze the data reported in this paper is available from the Lead Contact upon request.

EXPERIMENTAL MODEL AND SUBJECT DETAILS

Primary cell cultures—Isolation and differentiation of brown pre-adipocytes was performed as described before (Mills et al., 2018). Briefly, interscapular brown adipose tissue was dissected from 2 to 4-day old mice of mixed sexes and washed in PBS. Next, tissue was minced and digested for 45 min at 37 °C in isolation buffer containing 1.5 mg/mL collagenase B, 123 nM NaCl, 5 mM KCl, 1.3 mM $CaCl_2$, 5 mM glucose, 100 mM HEPES, and 4 % fatty acid free BSA. Solution was filtered through a 40 μm cell strainer and centrifuged at 600g for 5 min. The pellet of the stromal vascular fraction containing preadipocytes was resuspended in adipocyte culture medium (DMEM/F-12 Glutamax, ThermoFischer Scientific #10565018, supplemented with 10% FBS), plated in a 10 cm dish, and maintained at 37 °C in 10% CO_2. Medium was changed every other day until cells reach confluency. Brown adipocyte differentiation was induced with differentiation medium (cell culture medium containing 1 μM rosiglitazone, 0.5 mM IBMX, 5 μM dexamethasone, 0.114 μg/ml insulin, 1 nM T3, and 125 μM indomethacin) for 2 days. Media was refreshed every 48 h with the adipocyte culture medium containing 1 μM rosiglitazone, 1 nM T3, and 0.5 μg/mL insulin. Unless otherwise noted, experiments were performed day 7 after induction when cells were fully differentiated.

Mice—A heterogeneous cohort of 163 female DO mice (at the onset of HFD: 24 weeks, n=110; 18 months, n=10; 22 months, n=29; 28 months, n=14) were used to mimic the genetic and age heterogeneity of the human population. Male DO mice were not used due to cage aggression. These mice were developed in the Jackson Laboratory (Churchill et al., 2012) and descended from eight founder strains: A/J, C57BL/6J, 129S1/SvImJ, NOD/ShiLtJ, NZO/H1LtJ, CAST/EiJ, PWK/PhJ, and WSB/EiJ. These eight strains were crossed to generate the collaborative cross (CC) mice, which were inbred and fully genotyped. DO strains were developed by random crosses of CC lines, then maintained by continued random crosses without mating between siblings to retain the widest possible genetic diversity. The cohort in this study were ear-tagged and group-housed in a temperature-controlled (20–22 °C) room on a 6 am to 6 pm light/dark cycle upon arrival and fed a chow diet during acclimation before transferring to a thermoneutrality incubator (29 °C) to initiate experiments.

All other mice used in this study were of C57B/6J background. Mice of both bexes were group-housed in a temperature-controlled (20–22 °C) room on a 6 am to 6 pm light/dark cycle and fed a chow diet. Mice were of 8–10 weeks of age at the onset of experiments. The whole-body LETMD1 knockout mouse was generated by targeting exon 2 of its DNA using a synthetic sgRNA (AATGACGCCCCAAGAAACGA) complexed with a recombinant CRISPR/CAS9 protein (Synthego). This complex was injected into C57BL6/J embryos by the Transgenic Mouse Core at Dana-Faber/HMS. F0 founders were genotyped using oligos

surrounding exon 2. One founder was selected with a deletion of (5' – CTTCAAAGCTTCACCTTTCTCCGAAGGCGGACGTGAAGAACTTGATTTCTTACGT GGTGACC AAGACAAGAGCGATTAACGGATCGTACCATCGT −3'). F0 founder was bred back into C57BL/6J for two generations. All mouse experiments used littermate controls. All animal-related experiments were approved by Institutional Animal Care and Use Committee of the Beth Israel Deaconess Medical Center.

METHOD DETAILS

Genotyping of the DO cohort—Genomic DNA of this cohort (n=163) was extract from each mouse and genotyped at over 143,000 single nucleotide polymorphisms (SNPs) markers on the Giga-MUGA platform (Neogen) (Welsh and McMillan, 2012). All 163 samples passed SNP quality control metrics. For these samples, founder haplotypes were inferred from SNP probe intensities through a hidden Markov model using the R/qtl2 package (Broman et al., 2019), and then used to interpolate a grid of 64,000 evenly-spaced genetic intervals. Sample swap was checked based on pQTL peaks (pQTL mapping is described in the data analysis section below) similar to previous studies (Chick et al., 2016; Keele et al., 2021), which confirmed that none of the samples was swapped.

High fat feeding under thermoneutrality—At the onset of the HFD experiments, mice (housed five per cage) were transferred to a thermoneutrality incubator set at 29 °C and directly switched to a rodent high fat diet (OpenSource Diets, D12492) with 60% kcal% fat, 20% kcal% carbohydrate, and 20% kcal% protein (Kazak et al., 2017a). Mice were fed *ad libitum* with HFD for 8 weeks.

Body composition measurement—Body mass, fat mass, and lean mass were measured weekly starting from week 0 of HFD and during the entire high fat feeding experiment. Fat mass and lean mass were measured by an EchoMRI 3-in-1 body composition analyzer (Echo MRI LLC).

Fasting glucose measurement—Fasting glucose were measured at the onset and the end of HFD experiments, where mice were fasted in a fasting cage with an inedible bedding for 6 h between 9 am to 3 pm prior to glucose measurement with the OneTouch UltraMini blood glucose meter (LifeScan IP Holdings, LLC) as described before (Mills et al., 2018).

Metabolic cage experiment—At the end of the 8-week HFD experiments, mice were transferred to the Promethion indirect calorimetry cages (Sable Systems International), for a one-week indirect calorimetry experiment. Mice were singly housed in the metabolic cages and remained on HFD. Acclimation was performed for 24 h under thermoneutrality (TN, 29 °C), then the temperature was adjusted to room temperature (RT, 24 °C) for a day, cold (10 °C) for 3 hours, and TN for the rest of the experiment. The cold exposure was relatively mild to ensure that the older mice could survive. Experiments were designed according to the light dark cycle (6am to 6pm) in the room to ensure equal amount of data were collected during the day and at night. The following metabolic parameters were monitored: oxygen consumption (VO_2), carbon dioxide output (VCO_2), respiratory quotient (RQ), energy expenditure (EE), food consumption, and movement. Raw data was collected every 3

min, and converted using the ExpeData software package (Sable Systems International) to a format where columns were various metabolic parameters, and rows were data collected at all time points with 3-min intervals. All raw files and data points were manually inspected using the ExpeData software to ensure that no measurements that we reported in this study were made with malfunctioning modules. The same system was used for the indirect calorimetric studies on the LETMD1 knockout mice and SFXN5 knockdown mice detailed in sections below. For LETMD1 knockout experiments, mice were housed individually in metabolic chambers maintained at 30 °C under a 12 h light/dark cycle with free access to food and water. Intraperitoneal injection of CL316,243 (Sigma-Aldrich; 1 mg/kg) into mice was performed. For SFXN5 knockdown experiments, room temperature-housed mice were exposed with cold at 4 °C under a 12 h light/dark cycle with free access to food and water. Mice of both sexes were used for LETMD1 and SFXN5 studies.

Bomb calorimetry—Bomb calorimetry was conducted using a Parr 6725EA Semimicro Calorimeter and 1107 Oxygen Bomb. Fecal specimens were collected for each mouse immediately after the metabolic cage experiments. Collected samples were baked at 60 °C for 48 h to remove water content and then combusted to measure fecal energy content as heat of combustion (kcal/g). Experiments were performed in technical duplicates for each mouse.

BAT extraction—Immediately following metabolic cage experiments, mice were euthanized by rapid cervical dislocation, and both lobes of BAT were extracted and frozen in less than twenty seconds following euthanasia using the freeze-clamping method described previously (Xiao et al., 2020). Samples were stored in liquid nitrogen during extraction and later transferred to a −80 freezer for storage.

Sample preparation for proteomics—Prior to sample preparation, randomization was performed for all 163 samples to assign samples to tandem mass tags (TMT) plexes and channels. Physiological data described above were then overlaid onto the randomized sample assignments to check and ensure that no plex- or channel-based clustering of any physiological parameter was observed. All 163 DO BAT samples were weighed while frozen and lysed in the lysis buffer (100 mM 4-(2-hydroxyethyl)-1-piperazineethanesulfonic acid (HEPES) pH 8.5, 8 M urea, 2% SDS, 1p/15 mL Roche cOmplete™ protease inhibitors) to an initial concentration of ~ 4 – 8 mg/mL protein. Insoluble remnants were removed by centrifugation. A bicinchoninic acid (BCA) assay was performed to measure the exact protein concentration, and samples were diluted by the lysis buffer to 1 mg/mL protein based on the BCA results. A pooled sample, named the “bridge”, was then created by equally mixing 50 μg of proteins in each biological sample to represent the average BAT protein expression levels of the entire cohort. An aliquot of 200 μg of proteins from each sample was then subjected to disulfide reduction with 5 mM tris(2-carboxyethyl)phosphine (TCEP) at 37 °C for 1 h, followed by alkylation of free thiols by 25 mM iodoacetamide for 25 min at room temperature in the dark. Proteins were then precipitated by the methanol-chloroform method (Wessel and Flugge, 1984), resuspended in 200 mM N-(2-Hydroxyethyl)piperazine-N′-(3-propanesulfonic acid) (EPPS) buffer pH=8, and digested using a combination of Lys-C and trypsin at an enzyme-to-protein ratio of 1:100 overnight at 37 °C, followed by

an additional 4 h digestion with trypsin 1:100. Samples were then subjected to a microBCA measurement for peptide quantification, and 50 μg peptides (~50 μl of digestion solution +15 μL of acetonitrile (ACN)) from each sample were labeled by 100 μg of the TMTpro-16 reagents (Li et al., 2020b) for 1 h at room temperature following the streamlined-TMT protocol (Navarrete-Perea et al., 2018). TMT plexes and channels were determined by the randomized sample assignments as described above. The reaction was quenched using 5 μl of 5% hydroxylamine for 15 min. A ratio-check was performed by mixing 2 μL of peptides from each channel, desalted via StageTip, and analyzed by LC-MS. The remainder of samples in each plex of 15 biological samples plus 1 bridge sample were mixed in a tube containing 12 mL of 1% formic acid (FA), according to the total peptide loading ratios obtained from the ratio-check. The mixtures were then desalted with Waters SepPak cartridges, and the eluates were freeze-dried overnight using a speedvac system. Dried peptide samples (300 μg per TMT plex) were resuspended in the high-performance liquid chromatography (HPLC) buffer A containing 10 mM ammonium bicarbonate pH 8.0, 5% acetonitrile, and fractionated with basic pH reversed-phase HPLC using an Agilent 300 extend C18 column. A 50-min linear gradient in 13 – 43% buffer B (10 mM ammonium bicarbonate, 90% acetonitrile, pH 8.0) at a flow rate of 0.25 ml/min was used to separated peptides, and eluates were collected into a 96-deep-well plate. Samples were consolidated into 24 fractions and vacuum centrifuged to dryness. Each fraction was then desalted via StageTip, dried in a speedvac, and reconstituted in a solution containing 5% ACN and 4% FA for liquid chromatography tandem mass spectrometry (LC-MS/MS). Protein abundance in differentiated brown adipocytes (scramble, LETMD1^{KD}, and SFXN5^{KD}) and BAT tissue (control and ATP1A2^{KD}) were measured using the same workflow without the pooled "bridge" due to much smaller sample size. Mitochondria proteins were annotated based on MitoCarta 3.0 (Rath et al., 2021).

LC-MS/MS—To measure protein abundance, 2 μg of peptides in each fraction were loaded onto an in-house 100-μm capillary column packed with 35 cm of Accucore 150 resin (2.6 μm,150 Å). Measurements were made using an Orbitrap Eclipse Tribrid Mass Spectrometer (Thermo) coupled with an Easy-nLC 1200 (Thermo). A 180-min gradient consisting of 2% - 23% ACN, 0.125% FA at 500 nl/min flow rate was used to separate and analyze peptides. A FAIMSPro (Thermo) device was used for field asymmetric waveform ion mobility spectrometry (FAIMS) separation of precursors (Schweppe et al., 2019), and the device was operated with default settings and multiple compensation voltages (−40V/−60V/−80V). Under each voltage, peptide ions were collected in data-dependent mode using a mass range of m/z 400–1600 using 2 s cycles. Resolution for MS1 was set at 120,000. Singly-charged ions were not further sequenced, and multiply-charged ions were selected and subjected to fragmentation with standard automatic gain control (AGC) and 35% normalized collisional energy (NCE) for MS2, with a dynamic exclusion window of 120 s and maximum ion injection time of 50 ms. Quantification of TMT reporter ion were performed using the multinotch SPS-MS3 method (McAlister et al., 2014) with 45% NCE for MS3, which is optimized for TMTpro-16 reagents. For phosphoproteomics described in a section below, the same LC-MS/MS system and LC gradient were used for measurements. Unfractionated samples were analyzed twice, with FAIMS compensation voltages first at −35V/−45V/−55V then at −40V/−60V/−80V. Under each compensation voltage, peptide ions were collected

in data-dependent mode using a mass range of m/z 400–1600 using 1 s cycles with 50 ms maximun injection time. Dependent scans were performed on single charge state per precursor only using high resolution MS2. The isolation window was 0.5 Th, and activation type was HCD with 36% collisional energy. Maximum injection time was set to 150 ms for MS2 and TMTpro-16 reporter ions were quantified in MS2 as described previously (Schweppe et al., 2020).

Database searching—Raw files were first converted to mzXML, and searched using the Comet algorithm (Eng et al., 2013) on an in-house database search engine reported previously (Huttlin et al., 2010). Database searching included all mouse (Mus musculus) entries from UniProt (http://www.uniprot.org, downloaded July 29th, 2020) and the reversed sequences as well as common contaminants (keratins, trypsin, etc). Peptides were searched using the following parameters: 25 ppm precursor mass tolerance; 1.0 Da product ion mass tolerance; fully tryptic digestion; up to three missed cleavages; variable modification: oxidation of methionine (+15.9949); static modifications: TMTpro (+304.2071) on lysine and peptide N terminus, carboxyamidomethylation (+57.0214637236) on cysteines. For phosphoproteomics experiment described in a section below, 0.01 Da product mass tolerance was used, and an additional variable phosphorylation (+79.966 Da) on serine, threonine, or tyrosine was added. The target-decoy method was employed to control the false discovery rate (FDR) (Elias and Gygi, 2007; Huttlin et al., 2010; Peng et al., 2003) to < 1% on peptide level for each MS run using parameters such as XCorr, ΔCn, missed cleavages, peptide length, charge state and precursor mass accuracy. Peptides that are shorter than seven amino acids were discarded. Subsequently, all DO peptides that contained possible polymorphisms were filtered out using a method described in detail previously (Keele et al., 2021). Briefly, all founder strain protein sequences (A/J, C57BL/6J, 129S1/SvImJ, NOD/ShiLtJ, NZO/H1LtJ, CAST/EiJ, PWK/PhJ, and WSB/EiJ) were downloaded from Ensembl (Yates et al., 2020) and subjected to *in silico* tryptic digestion using the Protein Digestion Simulator (Pacific Northwest National Laboratory). A list containing peptides that are not shared across all founder strains was generated as the basis to filter out peptides with polymorphisms for the DO experiments. After filtering, proteins were assembled, and protein-level FDR was controlled to < 1% combining all MS runs. The Picked FDR method (Savitski et al., 2015) was employed to ensure the stringency of FDR control for our dataset that comprised of hundreds of MS runs. For phosphoproteomics runs, phosphorylation site localization was determined using the ModScore (AScore) algorithm (Beausoleil et al., 2006) where a score of 19 corresponds to 99% confidence that a given phosphorylation site was correctly localized.

TMT reporter-based quantification—TMT reporter ions were used for quantification of peptide abundance. Each reporter ion was scanned using a 0.003 Da window, and the most intense m/z was used. Isotopic impurities were corrected according to the manufacturer's specifications, and signal-to-noise ratio (S/N) was calculated. Peptides with summed S/N lower than 320 across 16 channels of each TMTpro16 plex or isolation specificity lower than 70% were discarded. The high confidence peptides were then used to quantify protein abundance by summing up S/N values for all peptides assigned to the same protein. Normalization for each TMT plex was then performed by adjusting protein

loadings to equal loading across all channels. A relative abundance for each protein across the DO cohort was obtained by calculating a sample-to-bridge ratio within each TMT plex for each channel of the fifteen biological samples (see sample preparation above for details of the bridge channel). This value was log2 transformed and used for data analysis described below. The values were analyzed in both raw and median-centered formats transformed following a workflow similar to that of a previous report (Nusinow et al., 2020). No batch effects were observed in either format via examinations using methods described previously (Nusinow and Gygi, 2020). Both formats returned nearly identical results for subsequent bioinformatic analyses, so here we reported raw relative protein abundance data in this work. To ensure stringency, for all the data analysis described below, we only used the 10,479 proteins that were quantified using peptides that were shared across all founder strains with a sum TMT S/N ≥ 320 and an isolation specificity ≥ 70%.

Mitochondrial isolation and tryptic digestion—Mitochondria were isolated following a well-established protocol (Cannon and Nedergaard, 2008) and further purified using a sucrose gradient as described previously (Sun et al., 2021). A total of 200 μg aliquots of sucrose purified mitochondria were resuspended in 20 mM HEPES pH 7.6 with 5 μg/ml of trypsin and in absence or presence of 10 ng/ml of digitonin for 30 min at room temperature. Sensitivity of proteins to trypsin digestion was assayed with SDS-PAGE followed by immunoblotting with the indicated antibodies. Mitochondria were treated rapidly with 1% SDS and boiled at 95 °C for 5 min to denature proteins and kept at −20 °C before western blot analysis.

Western blotting—Protein concentration was determined using the BCA assay (Pierce). A total of 10 μg of protein sample was loaded in each lane for western blot analysis unless otherwise indicated. Protein samples were denatured in Lamelli buffer and incubated at 37 °C for 20 minutes, resolved by 4–12% NuPAGE BisTris SDS-PAGE (Invitrogen), and transferred to a nitrocellulose membrane. Primary antibody incubations were performed in TBS containing 0.05% Tween (TBST) and 5% milk, for either 4 h at room temperature or overnight at 4 °C; secondary antibody incubations were performed using either HRP-conjugated or IRDye secondary antibodies in TBST with 5% milk for 2 h at room temperature, for visualization using chemiluminescence or fluorescence signal (LICOR).

Structured illumination microscopy—Stable integration of DNA sequence (obtained from the Bioplex 3.0 project (Huttlin et al., 2021)) that expresses LETMD1-HA or SFXN5-HA into U2OS cells was achieved by lentiviral transduction. These cells were then attached on high tolerance coverslips (MatTek #PCS-170–1818) and fixed by 3.7% freshly prepared and prewarmed paraformaldehyde (PFA) for 12 min at 37 °C with gentle agitation every 4 min. 3.7% PFA was prepared from 10% PFA stock (Electron Microscopy Science) by adding 2X Phosphate buffered saline (PBS) and then the distilled water to make an isotonic solution. The fixed cells were then gently washed with PBS (prewarmed to 37 °C), permeabilized by permeabilization solution (PBS supplemented with 0.1% Triton X-100) for 10 min at room temperature, and blocked by blocking solution (PBS supplemented with 0.1% Triton X-100 and 5% FBS) for 10 min at room temperature. For immunofluorescence staining, anti-HA mouse mAb (Abcam #ab18181) at 1:100 and anti-TOMM20 rabbit mAb

(Cell Signaling #42406) or anti-COX4 rabbit mAb (Cell Signaling #4850) at 1:100 in blocking solution were used for primary labeling of LETMD1-HA or SFXN5-HA and mitochondria, respectively, and anti-mouse Alexa Fluor 568 and anti-rabbit Alexa Fluor 647 at 1:500 (Invitrogen) were used for secondary labelling. Coverslips were mounted in ProLong Diamond Antifade Mountant (Invitrogen). Structured illumination microscopy (SIM) images were acquired on a GE DeltaVision OMX Blaze with Olympus 60X/1.42 Plan Apo oil-immersion objective, coupled to a front illuminated sCMOS camera (PCO) and an OMX laser system with 6 laser lines. For fluorescence detection of Alexa Fluor 568, 568 nm excitation laser, 571/19 (center wavelength/bandwidth) excitation filter, and 609/37 emission filter were used. For fluorescence detection of Alexa Fluor 647, 642-nm excitation laser, 645.5/15 excitation filter, and 683/40 emission filter were used. For each z-section, 15 raw images (three rotations with five phases each) were acquired. Spherical aberration was minimized using immersion oil matching (Hiraoka et al., 1990). Super-resolution images were computationally reconstructed from the raw data sets with a channel-specific, measured optical transfer function and a Wiener filter constant of 0.001 using CUDA-accelerated 3D-SIM reconstruction code (Gustafsson et al., 2008). TetraSpeck beads (Thermo Fisher) or a nano-grid control slide (GE) were used to measure axial and lateral chromatic misregistration, and experimental data sets were registered using the imwarp function in MATLAB (MathWorks). The processed images were analyzed using Fiji (Schindelin et al., 2012) and OME Remote Objects (OMERO) (Allan et al., 2012).

siRNA-mediated knockdown in brown adipocytes—Opti-MEM medium (Thermo Fisher Scientific #31985–070) was incubated with lipofectamine RNAiMAX (Life Technologies #13778–150) for 5 min at room temperature. In a separate tube, Opti-MEM medium was incubated with 1 μM ATP1A2 siRNA (Origene #SR421739) or scramble for 5 min. The siRNA mixture was then added dropwise to the lipofectamine mixture. Next, this final solution was added to the transfection plate (Isidor et al., 2016). After 25 min, brown adipocytes at day 5 of differentiation was suspended in cell differentiation medium using trypsin (Gibco #25200–056) and then plated in the transfection plate on top of the siRNA-lipofectamine mixture. The final concentration of siRNA was 90 nM. Measurement of intracellular levels of calcium, lipolysis rate, and cellular respirometry detailed in sections below were performed 48h after transfection with ATP1A2 siRNA or scramble. The knockdown of LETMD1 (IDT #mm.Ri.LETMD1.13) and SFXN5 (Horizon Discovery #J-057802–06) was conducted following the same procedure, except that the transfection was performed on brown adipocytes at day 4 (for LETMD1) or day 3 (for SFXN5) of differentiation and the cellular respirometry was performed 72 h (for LETMD1) or 96 h (for SFXN5) after transfection.

Protein overexpression in brown adipocytes—Overexpression of ATP1A2 in brown adipocytes were achieved by infecting cells at day 5 of differentiation with human ATP1A2 overexpression adenovirus (100 IFU/cell, Vector Biolabs #ADV-201680). Adenovirus overexpressing Cre or GFP was used as the control. Measurements of intracellular levels of calcium, PKA substrate phosphorylation, lipolysis rate, and cellular respirometry, were performed 48h after infection (which is day 8 after induction of cell differentiation).

Mitochondrial metabolomics—Mito-Tagged mice with the stop cassette deleted by a CMV-driven Cre were requested from the Whitehead Institute (Bayraktar et al., 2019). Pre-adipocytes were isolated from the BAT of 7-day old Mito-Tag mice and differentiated *in vitro* for 7 days. For norepinephrine-stimulated cells, 100 nM of norepinephrine was added to medium 15 min before rapid isolation of mitochondria. Isolation was performed as per the procedures described in previous studies (Chen et al., 2016; Sun et al., 2021) with minor modifications. Briefly, cells from each well of a 12-well plate were washed once with 0.5 ml cold PBS, once with 0.5 ml cold KPBS (136 mM KCl, 10 mM KH2PO4, pH 7.25), collected in 0.5 ml cold KPBS, transferred to a pre-chilled 2-ml homogenizer glass vessel (VWR, 89026–386), and disrupted by 20 stokes of a plain plunger (VWR, 89026–398) on ice. The resultant homogenate was poured into one 1.5-ml tube and centrifuged at 1,000g for 2 min at 4 °C, and the supernatant was collected and loaded onto Pierce anti-HA magnetic beads (Thermo Fisher Scientific) prewashed with cold KPBS. For cell lysate from one well of a 12-well dish, a 40 μl slurry of anti-HA beads was used. The lysate/anti-HA beads mixture was incubated on a rotator for 3.5 min in cold and pulse-spun to collect any residual liquid on the lid. The anti-HA beads were then collected on a magnet strip and the liquid was aspirated. The beads were quickly resuspended with 0.5 ml cold KPBS, split into 0.4 ml for metabolite extraction and 0.1 ml for western-blot analysis, and collected again on a magnet strip before the liquid was aspirated. Metabolites were eluted with 100 μl pre-chilled 80% MeOH with three internal standards (0.05 ng/ μL thymine-d_4, 0.05 ng/ μL inosine-$15N_4$, and 0.1 ng/ μL glycocholate-d_4), and proteins were eluted with 50 μl 1× NuPAGE LDS Sample Buffer (Invitrogen) supplemented with 1% β-mercaptoethanol (BME). The time spent on each step was strictly controlled across different purifications to minimize the variations in metabolites content. The metabolite extraction mixture was centrifuged at 17,000g for 10 min at 4 °C, and 80 μl of supernatant was collected, flash-frozen and stored in liquid nitrogen until further processing. Metabolite extracts were loaded onto a Luna-HILIC column (Phenomenex) on an UltiMate-3000 TPLRS LC. The starting gradient was 10% mobile phase A (20 mM ammonium acetate and 20 mM ammonium hydroxide in water) and 90% mobile phase B (10 mM ammonium hydroxide in 75:25 v/v ACN/MeOH). Metabolites were eluted with a 10-min linear gradient to 99% mobile phase A, and analyzed by a Q-Exactive™ HF-X mass spectrometer (Thermo). Negative and positive ion modes were used with full scan analysis over m/z 70–750 m/z at 60,000 resolution, 1e6 AGC, and 100 ms maximum ion accumulation time. Ion spray voltage was set at 3.8 kV, capillary temperature was at 350 °C, probe heater temperature was at 320 °C, sheath gas flow was set at 50, auxiliary gas was set at 15, and S-lens RF level was set at 40. Metabolite peaks were analyzed using TraceFinder (Thermo) software through a targeted approach. Peaks were matched to a metabolite library of ~800 validated metabolites on the LC-MS system, and peak area was used to quantify metabolite abundance.

Mitochondrial respiration—Mitochondria were isolated from *in vitro* differentiated brown adipocytes per established protocol (Cannon and Nedergaard, 2008; Shabalina et al., 2013) and equilibrated in a respiration assay buffer (125 mM Sucrose, 20 mM K+-TES pH 7.2, 2 mM $MgCl_2$, 1 mM EDTA, 4 mM KH_2PO_4, and 4% BSA) for 30 min on ice at a concentration of 1.5 mg/ml. 100 ul of the mitochondrial suspension (0.15 mg of mitochondria) was then loaded into the Oroboros O2K High-Resolution respirometer (2 ml

chamber filled with respiration assay buffer) for measurement of respiratory oxygen flux. A final concentration of 10 mM glycerol-3-phosphate or 5 mM pyruvate/2.5 mM malate (added with two consecutive injections of equal amount) was used to stimulate respiration. 10 mM GDP was then added to inhibit UCP1-dependent respiration. Maximal oxygen consumption rates were obtained by addition of CCCP to a final concentration of 40 uM.

Intracellular levels of Calcium—Differentiated brown adipocytes were loaded with Fluo-4 AM according to manufacturer's protocol (Fluo-4 Calcium Imaging Kit, ThermoFischer Scientific #F10489). Cells were imaged in Hank's balanced salt solution (HBSS) buffer containing 20 mM glucose. Cells were imaged using an inverted Nikon Ti2 fluorescence microscope. We used excitation wavelength of 480 nm and emission wavelength of 535 nm to measure changes in intracellular levels of calcium in response to norepinephrine stimulation. Cells were imaged every 4 sec for a total of 40 sec in baseline condition and for an additional 240 sec after norepinephrine administration. Images were analyzed using ImageJ (Schneider et al., 2012). After subtracting background fluorescence, Fluo-4 intensity was quantified for each cell and expressed as the relative change to baseline condition - F/F_0, where F_0 is the fluorescence level at 0 sec and F is the florescence level at any other time points.

Analysis of PKA substrate phosphorylation—Differentiated brown adipocytes ($ATP1A2^{KD}$ n = 4 and $ATP1A2^{OE}$ n = 4) described above were treated with 100 nM NE for 5 minutes in 10 cm dishes. Cells were lysed with 100 mM HEPES pH 8.5, 8 M urea, 2% SDS, 1p/15 mL Roche cOmplete™ protease inhibitors, 1p/15 mL Roche PhosSTOP™ phsophotase inhibitors to a concentration of ~ 1 mg/mL protein. Insoluble content was removed by centrifugation. Soluble content was reduced with 5 mM TCEP at 37 °C for 1 h, followed by alkylation of free thiols by 25 mM iodoacetamide for 25 min at room temperature in the dark. After methanol-chloroform precipitation, proteins were digested and TMT-labeled as described in the proteomics sample preparation section above. After labeling and mixing, the peptide mixtures were then desalted, dried, and subjected to enrichment of phosphopeptides via immobilized metal affinity chromatography (IMAC), using the High-Select Fe-NTA Phosphopeptide Enrichment Kit (Thermo) following the manufacturer's instructions. Enriched phosphopeptides were dried and desalted using StageTip, and analyzed as described above in the LC-MS/MS and database searching sections. PKA substrates were extracted from this dataset using the consensus -R/K-R/K-X-S/T- motif (Smith et al., 2011; Sun et al., 1991).

Lipolysis assay—Differentiated brown adipocytes were incubated in HBSS buffer (Corning #21–023- CV) supplemented with 20 mM glucose and treated as indicated before collection of HBSS buffer. Lipolysis rate was determined by measuring the amount of glycerol in the collected HBSS buffer using free glycerol reagent (Sigma Aldrich #F6428) relative to glycerol standard per manufacturer's protocol.

Cellular respirometry—Oxygen consumption rate (OCR) of differentiated brown adipocytes was determined using a Seahorse XF24 Extracellular Flux Analyzer as described before (Mills et al., 2018). Partially differentiated brown adipocytes were plated at a density

of 10,000 cells/well on day 3–5 of differentiation during transfection of siRNA. Experiments were performed on day 7–8. Before analysis, adipocyte culture medium was changed to DMEM respiration medium lacking $NaHCO_3$ (Sigma Aldrich #D5030) that contain 1.85 g/L NaCl, 3 mg/L phenol red, 2% fatty-acid-free BSA, and 1 mM sodium pyruvate, pH 7.4. For cellular respirometry in the characterization of LETMD1, an additional 10 mM Glucose and 2 mM Glutamine were added. Basal respiration was determined as OCR in the presence of substrate alone. After stimulation with norepinephrine, ATP-synthase-independent respiration was determined using 2.5 μM oligomycin (4 μM for LETMD1 and SFXN5 experiments). Maximal respiration was determined after addition of 2 μM DNP (5 μM CCCP for LETMD1 and SFXN5 experiments). Finally, rotenone (3 μM) and antimycin (3 μM) were used to abolish mitochondrial respiration.

Gene expression analysis—Gene expression analysis was performed as previously described (Reddy et al., 2020). Total RNA from cells was isolated using TRIzol (Ambion #15596018) with Qiagen RNA Mini Kit (QIAGEN #12183025). RNA content was quantified using a Nanodrop 2000 UV-visible spectrophotometer. cDNA synthesis was performed via reverse-transcription polymerase chain reaction (RT-PCR) using 100 ng of RNA for ATP1A2 experiments (500–1000 ng of RNA for LETMD1 experiments) and a high-capacity cDNA reverse transcription kit (ThermoFisher Scientific #4368813). cDNA was then used for real-time quantitative PCR (qPCR) analysis, which was performed in 384-well plate using GoTaq qPCR Master Mix (Promega #A6001). QuantStudio 6 Flex Real-Time PCR instrument (Applied Bio-systems) was used to run samples. Relative abundance of ATP1A2 was calculated by the delta-delta Ct methods using cyclophilin for ATP1A2 experiments (RPLP0 for LETMD1 experiments) as endogenous control.

Cold exposure in LETMD1 experiments—Mice were pre-acclimated at thermoneutrality (28–30°C) for two weeks and then shifted to 4°C. Body temperature was measured with a rectal probe (Physitemp, RET3) and a reader (Physitemp, BAT-12).

BAT SFXN5 knockdown *in vivo*—AAVs that carry shRNA that targets SFXN5 (target sequence: GCTGGTTCAGAAAGCAAACAA) and scrambled shRNA were prepared by VectorBuilder (VB900056–6989wbw and VB010000–0023jze, respectively) and injected to BAT as previously described with minor modifications (Zeng et al., 2019). 8-week-old male mice were anaesthetized with isoflurane and an incision was made above the interscapular area to expose the BAT. A dose of 1×10^{11} ifu of AAV (serotype 8) was injected into each BAT lobe and the incision was closed with suture. Mice received one injection of meloxicam (2 mg/kg) 24 h before surgery, and another injection immediately after surgery. Mice were allowed to recover for three weeks before analysis.

BAT ATP1A2 overexpression *in vivo*—BAT-specific ATP1A2 overexpression *in vivo* were achieved by injecting adeno-associated virus (AAV) with Cre-inducible expression of ATP1A2 (AAV8-CMV-DIO-mATP1A2, Vector Biolabs, custom order) into interscapular BAT of male Adiponectin-Cre C57BL/6 mice (Chen et al., 2017). AAV expressing GFP (AAV8-CAG-GFP-WPRE, Boston Children's Hospital Viral Core, custom order) was used as control. Briefly, mice received analgesics 16 h prior and after AVV injection. 8-week-old

Adiponectin-Cre mice were anesthetized with isoflurane and a small cut was made to expose the interscapular BAT. 6.0×10^{11} genomic copies (GC) were injected in the interscapular BAT of each mouse. Skin was closed with 3M Vetbond. Mice were allowed to recover for two weeks before analysis.

BAT ATP1A2 knockdown *in vivo*—BAT-specific ATP1A2 knockdown *in vivo* was achieved by injecting adeno-associated virus (AAV) with expression of ATP1A2 shRNA (AAV8-U6-GFP-ATP1A2-shRNA, VectorBuilder, custom order) into interscapular BAT of male C57BL/6 mice (Chen et al., 2017; Yoneshiro et al., 2019). AAV expressing a scramble shRNA (AAV8-U6-GFP-scramble-shRNA, VectorBuilder, custom order) was used as control. 6.0×10^{11} genomic copies (GC) were injected in the interscapular BAT of each mouse following procedures described in the section above. Mice were allowed to recover for two weeks before analysis.

HFD experiments for $ATP1A2^{OE}$ and $ATP1A2^{KD}$ mice—Mice were randomly split into littermate-matched groups to receive AAV injection as described above. Mice were fed with regular chow diet at RT for 2 weeks for recovery after the surgery and were checked regularly for well-being. HFD experiments were then carried out for 8 weeks at 29 °C in a thermoneutral incubator. Mice were singly caged, and body weight and food consumption were measured weekly during the experiment. Fat mass, and lean mass were measured at the onset of HFD feeding and at the end of the experiments via MRI described in a section above. The $ATP1A2^{KD}$ and scramble control cohorts were measured an additional time at 5 weeks of the experiment.

Histology experiments—Tissue fixation was performed with 10% neutral buffer formalin, embedded in paraffin, sectioned and mounted on glass slides and stained with haematoxylin and eosin or Sirius red. For LETMD1 experiments, we used a cohort of mixes sexes (n=3 per sex per genotype). For ATP1A2 experiments, male mice were used (n=3 each group). Images were collected with a Nikon Ti2 motorized inverted microscope and acquired with a Nikon DS-Fi1 color camera using NIS-Elements software. Whitening of brown adipocytes were graded by presence or absence of small lipid droplets as follow: grade 1 (> 80% small droplets in the view), grade 2 (50%−80%), grade3 (20%−50%), and grade 4 (< 20%). Samples were examined by a histologist at the DF/HCC Rodent Histopathology Core in a blinded experiment, which was able to assign grade 1 or 2 to all $ATP1A2^{KD}$ samples, and grade 3 or 4 to all control scramble samples.

Data analysis—All data analyses were performed using R 4.0.2 unless otherwise noted. (1) Kinship analysis of the cohort. Kinship of the subjects was analyzed through a genome scan by a linear mixed model provided by the R/QTL2 package (Broman et al., 2019), mapping the genetic relatedness among individuals. Briefly, the genotype probabilities were converted to allele probabilities, and the kinship matrix was calculated as the proportion of shared alleles. Effect of varying marker density across the genome was accounted for by using the probabilities along the grid of pseudomarkers. Positions that are not on the grid were omitted. (2) Comparison of the proteome coverages between OPABAT and datasets in the literature. Protein datasets were downloaded from these studies (Hu et al., 2020; Huttlin

et al., 2010; Kazak et al., 2015; Kazak et al., 2017b; Kazak et al., 2019; Li et al., 2020a; Williams et al., 2018; Yu et al., 2020; Zeng et al., 2019), and compared with OPABAT on proteome coverage across the spectrum of abundance. Mapping of low and high abundance proteins were performed by overlaying the datasets described above onto PaxDB (Wang et al., 2012), which is a database for absolute protein abundance measured in the literature. Overall proteome abundance variability comparison between DO and C57BL/6J cohorts was based on protein measurements in this work and those reported by (Yu et al., 2020). This dataset was selected because it harbored heterogeneity in age compositions that was similar to the current work. CV % of protein abundance was calculated for each protein across the whole cohort and used for comparison. (3) Mapping of OPABAT proteins to protein complex, pathway, and function in the literature. All 10,479 proteins measured in OPABAT were mapped to CORUM core complexes, KEGG pathways, and GO molecular functions (Ashburner et al., 2000; Gene Ontology, 2021; Giurgiu et al., 2019; Kanehisa et al., 2021; Ruepp et al., 2010). We only used stringently defined terms with fewer than or equal to 150 members, which account for 100% of all CORUM complexes, 81.1% of all KEGG pathways, and 96.3% of GO molecular function terms. This was to minimize the impact of overly broad terms on our analyses. Protein ID conversion during mapping was based on UniProt annotations (UniProt, 2021). (4) OPABAT co-operative protein network. Pearson's r was calculated between any possible protein pairs in our dataset. We required that the two proteins must be simultaneously quantified in at least fifty mice in our cohort. All correlations were then subjected to FDR control using r values as the input via R package 'fdrtool' (Strimmer, 2008a, b), as reported previously (Nusinow et al., 2020). Any correlation events with FDR $q \geq 0.05$ were filtered out of the network. As a result, all edges in the network had a Pearson's r higher than 0.75. These edges, along with the corresponding nodes (proteins) were used for network analysis. (5) Annotation of the edges in OPABAT using evidence in the literature. We considered four types of events that would serve as literature evidence for an OPABAT edge: physical interaction, pathway, and unambiguous gene ontology (cellular compartment excluded) and localization, where physical interaction would serve as the strongest evidence. We first mapped OPABAT onto CORUM (Giurgiu et al., 2019; Ruepp et al., 2010) and Bioplex (Huttlin et al., 2021; Huttlin et al., 2017; Huttlin et al., 2015), as these databases have confident experimental evidence to support true physical interactions. Physical interaction evidence reported in BioGRID (Oughtred et al., 2019), STRING (combined score > 700) (Szklarczyk et al., 2017), and MINT (Calderone et al., 2020) were then compiled and used for mapping. If the output from a database directly provides edges, then OPABAT edges were mapped onto established edges in the database; otherwise, edges were first constructed using nodes provided by the database and then used for mapping, such as CORUM. Pathway datasets were downloaded from UniProt, KEGG, and Reactome (Bateman et al., 2021; Jassal et al., 2020; Kanehisa et al., 2021). Both human and mouse pathways were used for this analysis. Subcellular localization data was downloaded from the Human Protein Atlas where subcellular localization data is supported by imaging experiments (Thul et al., 2017), and "cytosol" and "nucleus" were removed from this analysis due to their broad and ambiguous nature in explaining edges. Similarly, when mapping OPABAT edges onto GO biological processes and molecular functions (Ashburner et al., 2000; Gene Ontology, 2021), any terms that contain over 150 members were filtered out. Examples of established complexes or

pathways recapitulated in OPABAT were illustrated using Cytoscape 3.7.2 (Shannon et al., 2003). (6) Identification of co-operative proteins to established complexes and pathways. Established complexes were downloaded from CORUM core complexes, and we required that the complex must have at least 3 established subunits. Established pathways were downloaded from KEGG mouse dataset (pathway members ranged from 11 to 293). A Fisher's exact test, adapted from a previous work (Huttlin et al., 2020), was set up to calculate statistical enrichment of proteins' co-operativity with established networks. For a given established network, we tested its first-degree neighboring proteins for significant association with the network, which we termed co-operativity between the protein and the established network. For each individual test, we first counted the number of edges that linked the candidate protein to the established network; then counted the number of edges the established network had to other proteins that were not the candidate protein; then counted the number of edges the candidate protein had to other proteins that were not a part of the established network; lastly counted edges that did not involve the established network nor the candidate protein. These four numbers were used to set up the Fisher's exact test. This test was looped through all established networks (separately for complexes and pathways). The resulting p values were subjected to multiple testing correction using the Benjamini-Hochberg procedure (Benjamini and Hochberg, 1995), and any association with an adjusted p value < 0.05 was considered significant. (7) Identification of proteins that were co-operative with established key thermogenic factors. A list of key thermogenic factors was compiled from recent reputable reviews of thermogenesis and BAT biology (Chouchani et al., 2019; Ikeda et al., 2018; Rosen and Spiegelman, 2014; Wang and Seale, 2016). For each protein in the list, co-operative proteins were determined by extracting nodes with which the target protein formed significant co-operative edge (FDR $q < 0.05$) in OPABAT. Literature evidence of co-operativity edges was checked as described above. (8) Comparing phenotypic variability between C57BL/6 cohorts in the literature, the DO cohort, and human cohorts. C57BL/6 data was downloaded from the Mouse Phenome Database (http://www.jax.org/phenome, accessed April 30, 2022). Due to insufficient sample size for phenotypic measurements of aged mice with high fat feeding in the database, this comparison was restricted to young mature populations. All measurements for body weight (g) and fasting glucose (mg/dL) under the C57BL/6 category were downloaded, filtered to only contain mouse that were 16–29 weeks of age at the time of measurement, and compared with the 110 young mature mice (24 weeks of age) in OPABAT. For human data analysis, de-identified human data was obtained through a material transfer agreement with the Memorial Sloan Kettering Cancer Center (Becher et al., 2021). All available diagnoses presented in this dataset were status of cancer, congestive heart failure, atrial fibrillation, hypertension, type II diabetes, dyslipidemia, coronary artery disease, and cerebrovascular disease. Non-smoking patients were used for the analysis. Phenotypic data measured in patients with stage 4 cancer or other diseases mentioned above were excluded from this analysis to control for the effects of severe syndromes, such as cachexia, on metabolic phenotypes. Variability in human phenotypes were compared between genders, and compared to the variability in the outbred cohort of 163 mice. Differences in CV between the cohorts were tested using Feltz and Miller's test for the equality of coefficients of variation (Feltz and Miller, 1996). The R package cvequality (Version 0.2.0) was used to perform this test (Krishnamoorthy and Lee, 2014). (9) Protein and metabolic phenotype

QTL mapping. Ensembl version 102 gene and protein annotations were used in this analysis (Cunningham et al., 2022). For pQTL mapping, only the 8,923 proteins with at least 50% data completeness were included. A genome-wide pQTL scan was performed for each protein, testing a QTL effect at positions across the genome, using a model where the protein abundance was first transformed into a rank based on the rank-based inverse normal transformation (RINT) (Beasley et al., 2009; Keele et al., 2021). The purpose for using RINT for the QTL analysis was to reduce the chance of extreme observations resulting in false positives, especially in cases where there was a coincidence with rare founder haplotype alleles at the QTL location. pQTLs were mapped with the R/QTL2 package (Broman et al., 2019) using a linear mixed model with age as additive covariates and a random polygenic term to account for genetic relatedness among the 163 animals. Significance thresholds were estimated using 10,000 permutations (Churchill and Doerge, 1994). A LOD score was first calculated, which is log10 of the ratio of the probability that a QTL is present to the probability that a QTL is absent. For each protein, the peak with the highest LOD score was selected. Based on the LOD score, we calculated a genome-wide significance for each QTL by modeling the maximum LOD scores from the permutations using a generalized extreme value distributions (Dudbridge and Koeleman, 2004; Valdar et al., 2009) in order to compute genome-wide permutation p-value for each protein. These permutation p values were further adjusted by the Benjamini-Hochberg procedure. All detected pQTLs were classified as local if their position was within a ±5 Mbp window centered around the coding gene. If they did not fall within this local window, they were classified as distant. Phenotype QTLs were mapped using the same method described above without assigning local or distant QTLs. (10) Analysis to select founder and CC strains for specific phenotypic outputs. On the basis of the mapped QTLs, we first analyzed the founder strain allelic effects at the QTL position. Founder strains were ranked from the most negative to most positive allelic contributors to the QTL. We then queried the QTL location in the CC Giga-MUGA genotyping database (http://csbio.unc.edu/CCstatus/CCGenomes/) to map CC strains which are homozygous for the founder strain of interest at the QTL position. (11) Correlation between protein abundance and physiological parameters. All body compositional and metabolic parameters measured in the DO cohort were used for this analysis. For each of the parameters measured in metabolic cages, an average is calculated for every segment of the experiment. For instance, all VO_2 measurements during the day at 24 °C were averaged to calculate VO_2 RT/day. Data collected during transitions, e.g., changing temperature from 29 °C to 24 °C, was discard prior to this calculation. Only data collected after stabilization was used. All physiological parameters were z-scored and correlated with the log2 transformed relative abundance of each protein measured in OPABAT, and a Pearson's r was calculated. Of note, we also performed the analysis using Spearman's rank correlation coefficient as the matrix and obtained very similar results. If a protein and the physiological parameter were simultaneously measured in fewer than half of the mice in the DO cohort, then the correlation was not calculated. For each parameter, we rankordered all proteins according to their Pearson's r, and considered $|r| \geq 0.4$ and $p < 0.05$ significantly correlated. Established key proteins in BAT thermogenesis were examined for potential correlation with physiological parameters in the DO cohort. In order to measure the similarity between protein correlators of different physiological parameters, the Jaccard similarity was calculated by dividing the number of protein correlators in the

intersection by the number of protein correlators in the union of two given parameters. In parallel to Pearson correlation analysis, we also performed linear regression using the Lasso method (Tibshirani, 1996) through the R package 'glmnet'. We again required that proteins and physiological parameters must be measured simultaneously in at least half of the cohort. Log2 transformed relative protein abundance was used as the matrix to predict physiological parameters. A seed number of 100,000,000 was set to ensure reproducibility of the analysis. Weights were set to 1 for all observations. Cross validation was performed using squared-error. Data points were split to 90% and 10%, where for each iteration, 90% of the data was used for modeling, and 10% was used for validation. Five values, 0, 0.25, 0.5, 0.75, and 1 were set for mixing the relaxed fit with the regularized fit. To ensure stringency of the output, proteins with none-zero coefficients at one standard error away from the minimum cross-validation error (lamda.1se, which gives the most regularized model) were used as the output. A permutation test was carried out to test statistical significance of this analysis by random rearrangements of abundance values to proteins, and it was repeated 10,000 times. Permutation $p < 0.05$ was considered significant. (12) Estimation of cell populations. Cell types used for this analysis were determined referring to single nucleus RNA-seq data of BAT reported in the literature (Sun et al., 2020). Cell types were further clustered as follow: adipocytes- adipocytes; lymphoid- B-cells, $CD4^+$ T cells, $CD8^+$ T cells; myeloid-dendritic cells, monocytes, macrophages; vasclular- endothelial cells; preadipocyte/fibroblast: preadipocytes, fibroblasts. Prior to digital cytometry, proteins in our dataset were filtered based on correlation with mRNA in the literature (Chick et al., 2016). Proteins with lower than 0.2 Pearson's correlation were removed from this analysis. Digital cytometry of our proteomics data was performed using CYBERSORTx algorithm (Newman et al., 2019) with signature matrix obtained from the R package "celldex" (Aran et al., 2019; Consortium, 2012; Martens and Stunnenberg, 2013). Length-normalized and batch-corrected TMT signal-to-noise ratios for proteins in all samples were used as the mixture matrix. The "Impute Cell Fractions" module was used for this analysis using default settings. Cell fractions for each sample were compared to the population mean to measure the variation of cell fractions across the whole cohort. These values were then Log2 transformed, and correlated with z-scored phenotypic measurements to investigate the correlation between cell fractions and phenotypic outputs. The results were then compared with the BATLAS dataset (Perdikari et al., 2018). (13) Analysis of human tissue enrichment for OPABAT correlators of metabolic physiology. De-identified human BAT and SAT transcript data from 10 patients was measured by microarray. This study followed the institutional guidelines and was approved by the Human Studies Institutional Review Boards of Beth Israel Deaconess Medical Center and Joslin Diabetes Center. Details on procedures of the human adipose tissue collection were described previously (Cypess et al., 2013). The human BAT was collected from the deep neck region, and the human SAT was from the superficial/subcutaneous neck region. Differential expression of transcripts was tested using a two-tailed ttest, and $p < 0.05$ was assigned significant. OPABAT correlators of metabolic physiology were then mapped onto this dataset. A Fisher's exact test was set up by counting the number of proteins on the basis of whether or not they were metabolic phenotype correlators in OPABAT, and whether or not their transcript abundance was significantly higher in one tissue. This test was performed for both BAT and SAT, and tissue enrichment was determined by $p < 0.05$ in the Fisher's exact test. (14) Mapping

OPABAT protein correlators onto human transcript correlators of metabolic physiology. Twenty women with overweight or obesity participated in a clinical trial conducted at Washington University School of Medicine in St. Louis (ClinicalTrials.gov NCT02786251). All participants completed: i) a comprehensive screening evaluation that included a medical history and physical examination, standard blood tests, and a 75-g oral glucose tolerance test; ii) a BAT assessment visit to assess BAT volume and activity by using positron emission tomography-computed tomography (PET-CT) imaging of the neck and torso after intravenous 2-deoxy-2-[^{18}F]-fluoro-glucose (^{18}F-FDG) injection and a 6-h exposure to mild cold (Chondronikola et al., 2014; Chondronikola et al., 2016); and iii) a biopsy visit that involved sampling of the supraclavicular adipose tissue depot (Chondronikola et al., 2015)-where BAT is localized in people - after 6-h of exposure to thermoneutrality (room temperature of ~26–28 °C). BAT transcript abundance was measured by bulk RNA-seq, and data was presented as TPM (Transcripts Per Million). For transcripts with at least 50% data completeness, transcript abundance was correlated with z-transformed phenotypic data for each parameter, and correlations with |Pearson's r| ≥ 0.4 and $p < 0.05$ were considered significant. OPABAT metabolic physiology correlators were then mapped onto this dataset to examine the recapitulation of OPABAT correlators in human. This analysis was looped through all possible pairs of phenotypes (eg., body weight in OPABAT versus BMI in human). For each pair, false discovery was controlled by permutation test with 10,000 iterations through label randomization of the proteins/transcripts, pairs with $p < 0.05$ was considered significant and reported in our work. The phenotypic and transcript data for the human SAT cohort was requested from a prior work (Emont et al., 2022). The data was analyzed using the same workflow as described for the human BAT cohort. (15) Association between disease networks and proteins that correlate with metabolic phenotypes. Established disease networks were downloaded from DisGeNET (Pinero et al., 2020; Pinero et al., 2021), and networks with fewer than 3 members were removed. For any given metabolic phenotype, a Fisher's exact test was then set up, counting number of proteins that belong to the following categories: proteins that correlate with the given phenotype and belong to the candidate disease network; proteins that correlate with this phenotype but do not belong to the candidate disease network; proteins that do not correlate with this phenotype but belong to the candidate disease network; proteins that neither correlate with this phenotype nor belong to the candidate disease network. Both enrichment and depletion were considered. The test was looped through all disease networks and metabolic phenotypes. An additional loop was performed testing the association between disease networks and all protein correlates of metabolic phenotypes. The resulting p values from all tests were then subjected to multiple test correction using the Benjamini-Hochberg procedure, and any association with an adjusted p value < 0.05 was considered significant. BioRender was used for illustration.

OPABAT web application—The OPABAT web application (https://wren.hms.harvard.edu/opabat/) runs on a Linux virtual machine (Ubuntu 14.04.5 LTS, Apache 2.4.7). The application is written in R Shiny, and data visualizations were made possible with these packages: 'shiny', 'tidyverse', 'ggpubr', 'visNetwork', 'png', 'dqshiny', 'DT', 'gsubfn', 'shinymanager' (Wickham et al., 2019).

QUANTIFICATION AND STATISTICAL ANALYSIS

Quantification and statistical analysis pipelines are described in the sections above. Data analysis was performed in Excel, R, Prism, and ExpeData as described above. All data (unless otherwise noted) were presented as mean ± S.E.M. All p values (unless otherwise noted) were calculated using Student's t test for pairwise comparison of variables, and two-way ANOVA for comparisons with both group variables and time points as described in the figure legends. Comparison of CVs were performed using Feltz and Miller's test for the equality of coefficients of variation (Feltz and Miller, 1996). For multiple testing correction, the Benjamini-Hochberg procedure was used, and a p value < 0.05 was considered significant. For false discovery rate control, an FDR $q < 0.05$ was set as the cutoff. Unless otherwise noted, all stated replicates were biological replicates.

ADDITIONAL RESOURCES

OPABAT dataset is provided as an interactive web resource at https://wren.hms.harvard.edu/opabat/. The QTL mapping data can also be accessed at https://churchilllab.jax.org/qtlviewer/Chouchani/OPABAT.

Supplementary Material

Refer to Web version on PubMed Central for supplementary material.

Acknowledgments

Jonathon O'Brien, Qing Yu, Miljan Kuljanin, Hans-Georg Sprenger, Blythe P Durbin-Johnson, Raja Ramaswamy, Lin Shao, Talley Lambert, Jennifer Waters, J. Daniel Giardina, Yassir Al-Sayagh, Rachel Hatridge, Matthew Vincent, Nathan Bulloch, John Szpyt, the Harvard Chan Bioinformatics Core, and the Harvard Nikon Imaging Center are acknowledged for technical assistance and helpful discussions. This work was supported by a sponsored research agreement from Calico Life Sciences LLC (E.T.C.), the Claudia Adams Barr Program (E.T.C.), the Lavine Family Fund (E.T.C), the Pew Charitable Trust (E.T.C.), NIH DK123095 (E.T.C.), NIH K99AG073461 (H.X.), National Cancer Center (H.X.), NHGRI HG006673 (E.L.H. and S.P.G.), P30 DK56341 (S.K.), BJC Foundation (S.K.), the USDA-NIFA CA-D-NTR-2618-H (M.C.), American Heart Association 17POST33060003 (M.C.) and 926512 (L.H.M.B.), MIH RC2 DK116691 (E.D.R.), and NIH R01GM070683 (G.A.C.).

References

Allan C, Burel JM, Moore J, Blackburn C, Linkert M, Loynton S, Macdonald D, Moore WJ, Neves C, Patterson A, et al. (2012). OMERO: flexible, model-driven data management for experimental biology. Nat Methods 9, 245–253. [PubMed: 22373911]

Antonicka H, Lin ZY, Janer A, Aaltonen MJ, Weraarpachai W, Gingras AC, and Shoubridge EA (2020). A High-Density Human Mitochondrial Proximity Interaction Network. Cell Metab 32, 479–497 e479. [PubMed: 32877691]

Aran D, Looney AP, Liu L, Wu E, Fong V, Hsu A, Chak S, Naikawadi RP, Wolters PJ, Abate AR, et al. (2019). Reference-based analysis of lung single-cell sequencing reveals a transitional profibrotic macrophage. Nat Immunol 20, 163–172. [PubMed: 30643263]

Ashburner M, Ball CA, Blake JA, Botstein D, Butler H, Cherry JM, Davis AP, Dolinski K, Dwight SS, Eppig JT, et al. (2000). Gene ontology: tool for the unification of biology. The Gene Ontology Consortium. Nat Genet 25, 25–29. [PubMed: 10802651]

Barroso I, and McCarthy MI (2019). The Genetic Basis of Metabolic Disease. Cell 177, 146–161. [PubMed: 30901536]

Bateman A, Martin MJ, Orchard S, Magrane M, Agivetova R, Ahmad S, Alpi E, Bowler-Barnett EH, Britto R, Bursteinas B, et al. (2021). UniProt: the universal protein knowledgebase in 2021. Nucleic Acids Research 49, D480–D489. [PubMed: 33237286]

Bayraktar EC., Baudrier L., Ozerdem C., Lewis CA., Chan SH., Kunchok T., Abu-Remaileh M., Cangelosi AL., Sabatini DM., Birsoy K., et al. . (2019). MITO-Tag Mice enable rapid isolation and multimodal profiling of mitochondria from specific cell types in vivo. Proc Natl Acad Sci U S A 116, 303–312. [PubMed: 30541894]

Beasley TM, Erickson S, and Allison DB (2009). Rank-based inverse normal transformations are increasingly used, but are they merited? Behav Genet 39, 580–595. [PubMed: 19526352]

Beausoleil SA, Villen J, Gerber SA, Rush J, and Gygi SP (2006). A probability-based approach for high-throughput protein phosphorylation analysis and site localization. Nature Biotechnology 24, 1285–1292.

Becher T, Palanisamy S, Kramer DJ, Eljalby M, Marx SJ, Wibmer AG, Butler SD, Jiang CES, Vaughan R, Schoder H, et al. (2021). Brown adipose tissue is associated with cardiometabolic health. Nature Medicine 27, 58-+.

Benjamini Y, and Hochberg Y. (1995). Controlling the False Discovery Rate - a Practical and Powerful Approach to Multiple Testing. J R Stat Soc B 57, 289–300.

Bergstrom A, McCarthy SA, Hui R, Almarri MA, Ayub Q, Danecek P, Chen Y, Felkel S, Hallast P, Kamm J, et al. (2020). Insights into human genetic variation and population history from 929 diverse genomes. Science 367.

Bludau I. (2021). Discovery-Versus Hypothesis-Driven Detection of Protein-Protein Interactions and Complexes. Int J Mol Sci 22.

Bogue MA, Philip VM, Walton DO, Grubb SC, Dunn MH, Kolishovski G, Emerson J, Mukherjee G, Stearns T, He H, et al. (2020). Mouse Phenome Database: a data repository and analysis suite for curated primary mouse phenotype data. Nucleic Acids Res 48, D716–D723. [PubMed: 31696236]

Bordicchia M, Liu D, Amri EZ, Ailhaud G, Dessi-Fulgheri P, Zhang C, Takahashi N, Sarzani R, and Collins S. (2012). Cardiac natriuretic peptides act via p38 MAPK to induce the brown fat thermogenic program in mouse and human adipocytes. J Clin Invest 122, 1022–1036. [PubMed: 22307324]

Broman KW, Gatti DM, Simecek P, Furlotte NA, Prins P, Sen S, Yandell BS, and Churchill GA (2019). R/qtl2: Software for Mapping Quantitative Trait Loci with High-Dimensional Data and Multiparent Populations. Genetics 211, 495–502. [PubMed: 30591514]

Calderone A, Iannuccelli M, Peluso D, and Licata L. (2020). Using the MINT Database to Search Protein Interactions. Curr Protoc Bioinformatics 69, e93. [PubMed: 31945268]

Cannon B, and Nedergaard J. (2008). Studies of thermogenesis and mitochondrial function in adipose tissues. Methods Mol Biol 456, 109–121. [PubMed: 18516556]

Chen CY, Gherzi R, Ong SE, Chan EL, Raijmakers R, Pruijn GJ, Stoecklin G, Moroni C, Mann M, and Karin M. (2001). AU binding proteins recruit the exosome to degrade ARE-containing mRNAs. Cell 107, 451–464. [PubMed: 11719186]

Chen WW, Freinkman E, Wang T, Birsoy K, and Sabatini DM (2016). Absolute Quantification of Matrix Metabolites Reveals the Dynamics of Mitochondrial Metabolism. Cell 166, 1324–1337 e1311. [PubMed: 27565352]

Chen Y, Zeng X, Huang X, Serag S, Woolf CJ, and Spiegelman BM (2017). Crosstalk between KCNK3-Mediated Ion Current and Adrenergic Signaling Regulates Adipose Thermogenesis and Obesity. Cell 171, 836-+.

Chick JM, Munger SC, Simecek P, Huttlin EL, Choi K, Gatti DM, Raghupathy N, Svenson KL, Churchill GA, and Gygi SP (2016). Defining the consequences of genetic variation on a proteome-wide scale. Nature 534, 500–505. [PubMed: 27309819]

Choi KM., Kim JH., Kong X., Isik M., Zhang J., Lim HW., and Yoon JC. (2021). Defective brown adipose tissue thermogenesis and impaired glucose metabolism in mice lacking Letmd1. Cell Rep 37, 110104.

Chondronikola M, Annamalai P, Chao T, Porter C, Saraf MK, Cesani F, and Sidossis LS (2015). A percutaneous needle biopsy technique for sampling the supraclavicular brown adipose tissue depot of humans. Int J Obes (Lond) 39, 1561–1564. [PubMed: 25920777]

Chondronikola M, Volpi E, Borsheim E, Porter C, Annamalai P, Enerback S, Lidell ME, Saraf MK, Labbe SM, Hurren NM, et al. (2014). Brown adipose tissue improves whole-body glucose homeostasis and insulin sensitivity in humans. Diabetes 63, 4089–4099. [PubMed: 25056438]

Chondronikola M, Volpi E, Borsheim E, Porter C, Saraf MK, Annamalai P, Yfanti C, Chao T, Wong D, Shinoda K, et al. (2016). Brown Adipose Tissue Activation Is Linked to Distinct Systemic Effects on Lipid Metabolism in Humans. Cell Metab 23, 1200–1206. [PubMed: 27238638]

Chouchani ET, Kazak L, and Spiegelman BM (2019). New Advances in Adaptive Thermogenesis: UCP1 and Beyond. Cell Metab 29, 27–37. [PubMed: 30503034]

Churchill GA, and Doerge RW (1994). Empirical threshold values for quantitative trait mapping. Genetics 138, 963–971. [PubMed: 7851788]

Churchill GA, Gatti DM, Munger SC, and Svenson KL (2012). The Diversity Outbred mouse population. Mamm Genome 23, 713–718. [PubMed: 22892839]

Consortium EP (2012). An integrated encyclopedia of DNA elements in the human genome. Nature 489, 57–74. [PubMed: 22955616]

Cunningham F, Allen JE, Allen J, Alvarez-Jarreta J, Amode MR, Armean IM, Austine-Orimoloye O, Azov AG, Barnes I, Bennett R, et al. (2022). Ensembl 2022. Nucleic Acids Res 50, D988–D995. [PubMed: 34791404]

Cypess AM, and Kahn CR (2010). Brown fat as a therapy for obesity and diabetes. Curr Opin Endocrinol 17, 143–149.

Cypess AM, White AP, Vernochet C, Schulz TJ, Xue R, Sass CA, Huang TL, Roberts-Toler C, Weiner LS, Sze C, et al. (2013). Anatomical localization, gene expression profiling and functional characterization of adult human neck brown fat. Nat Med 19, 635–639. [PubMed: 23603815]

de Jong JMA, Sun W, Pires ND, Frontini A, Balaz M, Jespersen NZ, Feizi A, Petrovic K, Fischer AW, Bokhari MH, et al. (2019). Human brown adipose tissue is phenocopied by classical brown adipose tissue in physiologically humanized mice. Nat Metab 1, 830–843. [PubMed: 32694768]

Doganli C, Kjaer-Sorensen K, Knoeckel C, Beck HC, Nyengaard JR, Honore B, Nissen P, Ribera A, Oxvig C, and Lykke-Hartmann K. (2012). The alpha2Na+/K+-ATPase is critical for skeletal and heart muscle function in zebrafish. J Cell Sci 125, 6166–6175. [PubMed: 23097043]

Dudbridge F, and Koeleman BP (2004). Efficient computation of significance levels for multiple associations in large studies of correlated data, including genomewide association studies. Am J Hum Genet 75, 424–435. [PubMed: 15266393]

Elias JE, and Gygi SP (2007). Target-decoy search strategy for increased confidence in large-scale protein identifications by mass spectrometry. Nature Methods 4, 207–214. [PubMed: 17327847]

Emont MP, Jacobs C, Essene AL, Pant D, Tenen D, Colleluori G, Di Vincenzo A, Jorgensen AM, Dashti H, Stefek A, et al. (2022). A single-cell atlas of human and mouse white adipose tissue. Nature 603, 926–933. [PubMed: 35296864]

Eng JK, Jahan TA, and Hoopmann MR (2013). Comet: An open-source MS/MS sequence database search tool. Proteomics 13, 22–24. [PubMed: 23148064]

Feltz CJ, and Miller GE (1996). An asymptotic test for the equality of coefficients of variation from k populations. Stat Med 15, 646–658. [PubMed: 8731006]

Frazer KA, Eskin E, Kang HM, Bogue MA, Hinds DA, Beilharz EJ, Gupta RV, Montgomery J, Morenzoni MM, Nilsen GB, et al. (2007). A sequence-based variation map of 8.27 million SNPs in inbred mouse strains. Nature 448, 1050–1053. [PubMed: 17660834]

Geiger T, Velic A, Macek B, Lundberg E, Kampf C, Nagaraj N, Uhlen M, Cox J, and Mann M. (2013). Initial quantitative proteomic map of 28 mouse tissues using the SILAC mouse. Mol Cell Proteomics 12, 1709–1722. [PubMed: 23436904]

Gene Ontology C. (2021). The Gene Ontology resource: enriching a GOld mine. Nucleic Acids Res 49, D325–D334. [PubMed: 33290552]

Giurgiu M., Reinhard J., Brauner B., Dunger-Kaltenbach I., Fobo G., Frishman G., Montrone C., and Ruepp A. (2019). CORUM: the comprehensive resource of mammalian protein complexes-2019. Nucleic Acids Res 47, D559–D563. [PubMed: 30357367]

Golovina VA, Song H, James PF, Lingrel JB, and Blaustein MP (2003). Na+ pump alpha(2)-subunit expression modulates Ca2+ signaling. Am J Physiol-Cell Ph 284, C475–C486.

Gustafsson MG, Shao L, Carlton PM, Wang CJ, Golubovskaya IN, Cande WZ, Agard DA, and Sedat JW (2008). Three-dimensional resolution doubling in wide-field fluorescence microscopy by structured illumination. Biophys J 94, 4957–4970. [PubMed: 18326650]

Hiraoka Y, Sedat JW, and Agard DA (1990). Determination of three-dimensional imaging properties of a light microscope system. Partial confocal behavior in epifluorescence microscopy. Biophys J 57, 325–333. [PubMed: 2317554]

Hu B, Jin C, Zeng X, Resch JM, Jedrychowski MP, Yang Z, Desai BN, Banks AS, Lowell BB, Mathis D, et al. (2020). gammadelta T cells and adipocyte IL-17RC control fat innervation and thermogenesis. Nature 578, 610–614. [PubMed: 32076265]

Huttlin EL, Bruckner RJ, Navarrete-Perea J, Cannon JR, Baltier K, Gebreab F, Gygi MP, Thornock A, Zarraga G, Tam S, et al. (2021). Dual proteome-scale networks reveal cell-specific remodeling of the human interactome. Cell 184, 3022-+.

Huttlin EL, Bruckner RJ, Navarrete-Perea J, Cannon JR, Baltier K, Gebreab F, Gygi MP, Thornock A, Zarraga G, Tam S, et al. (2020). Dual Proteome-scale Networks Reveal Cell-specific Remodeling of the Human Interactome. bioRxiv, 2020.2001.2019.905109.

Huttlin EL, Bruckner RJ, Paulo JA, Cannon JR, Ting L, Baltier K, Colby G, Gebreab F, Gygi MP, Parzen H, et al. (2017). Architecture of the human interactome defines protein communities and disease networks. Nature 545, 505–509. [PubMed: 28514442]

Huttlin EL, Jedrychowski MP, Elias JE, Goswami T, Rad R, Beausoleil SA, Villen J, Haas W, Sowa ME, and Gygi SP (2010). A tissue-specific atlas of mouse protein phosphorylation and expression. Cell 143, 1174–1189. [PubMed: 21183079]

Huttlin EL, Ting L, Bruckner RJ, Gebreab F, Gygi MP, Szpyt J, Tam S, Zarraga G, Colby G, Baltier K, et al. (2015). The BioPlex Network: A Systematic Exploration of the Human Interactome. Cell 162, 425–440. [PubMed: 26186194]

Ikeda K, Kang QQ, Yoneshiro T, Camporez JP, Maki H, Homma M, Shinoda K, Chen Y, Lu XD, Maretich P, et al. (2017). UCP1-independent signaling involving SERCA2b-mediated calcium cycling regulates beige fat thermogenesis and systemic glucose homeostasis. Nature Medicine 23, 1454–+.

Ikeda K, Maretich P, and Kajimura S. (2018). The Common and Distinct Features of Brown and Beige Adipocytes. Trends Endocrinol Metab 29, 191–200. [PubMed: 29366777]

Isidor MS, Winther S, Basse AL, Petersen MC, Cannon B, Nedergaard J, and Hansen JB (2016). An siRNA-based method for efficient silencing of gene expression in mature brown adipocytes. Adipocyte 5, 175–185. [PubMed: 27386153]

Izquierdo AG, Crujeiras AB, Casanueva FF, and Carreira MC (2019). Leptin, Obesity, and Leptin Resistance: Where Are We 25 Years Later? Nutrients 11.

Jassal B, Matthews L, Viteri G, Gong C, Lorente P, Fabregat A, Sidiropoulos K, Cook J, Gillespie M, Haw R, et al. (2020). The reactome pathway knowledgebase. Nucleic Acids Res 48, D498–D503. [PubMed: 31691815]

Kanehisa M, Furumichi M, Sato Y, Ishiguro-Watanabe M, and Tanabe M. (2021). KEGG: integrating viruses and cellular organisms. Nucleic Acids Res 49, D545–D551. [PubMed: 33125081]

Kazak L, Chouchani ET, Jedrychowski MP, Erickson BK, Shinoda K, Cohen P, Vetrivelan R, Lu GZ, Laznik-Bogoslavski D, Hasenfuss SC, et al. (2015). A creatine-driven substrate cycle enhances energy expenditure and thermogenesis in beige fat. Cell 163, 643–655. [PubMed: 26496606]

Kazak L., Chouchani ET., Lu GZ., Jedrychowski MP., Bare CJ., Mina AI., Kumari M., Zhang S., Vuckovic I., Laznik-Bogoslavski D., et al. . (2017a). Genetic Depletion of Adipocyte Creatine Metabolism Inhibits Diet-Induced Thermogenesis and Drives Obesity (vol 26, pg 1, 2017). Cell Metabolism 26, 693–693. [PubMed: 28978428]

Kazak L, Chouchani ET, Stavrovskaya IG, Lu GZ, Jedrychowski MP, Egan DF, Kumari M, Kong X, Erickson BK, Szpyt J, et al. (2017b). UCP1 deficiency causes brown fat respiratory chain depletion and sensitizes mitochondria to calcium overload-induced dysfunction. Proc Natl Acad Sci U S A 114, 7981–7986. [PubMed: 28630339]

Kazak L, Rahbani JF, Samborska B, Lu GZ, Jedrychowski MP, Lajoie M, Zhang S, Ramsay LC, Dou FY, Tenen D, et al. (2019). Ablation of adipocyte creatine transport impairs thermogenesis and causes diet-induced obesity. Nat Metab 1, 360–370. [PubMed: 31161155]

Keele GR, Zhang T, Pham DT, Vincent M, Bell TA, Hock P, Shaw GD, Paulo JA, Munger SC, Pardo-Manuel de Villena F, et al. (2021). Regulation of protein abundance in genetically diverse mouse populations. Cell Genomics 1, 100003.

Krishnamoorthy K, and Lee M. (2014). Improved tests for the equality of normal coefficients of variation. Computation Stat 29, 215–232.

Kustatscher G, Collins T, Gingras AC, Guo T, Hermjakob H, Ideker T, Lilley KS, Lundberg E, Marcotte EM, Ralser M, et al. (2022a). An open invitation to the Understudied Proteins Initiative. Nat Biotechnol 40, 815–817. [PubMed: 35534555]

Kustatscher G, Collins T, Gingras AC, Guo T, Hermjakob H, Ideker T, Lilley KS, Lundberg E, Marcotte EM, Ralser M, et al. (2022b). Understudied proteins: opportunities and challenges for functional proteomics. Nat Methods.

Kustatscher G, Grabowski P, Schrader TA, Passmore JB, Schrader M, and Rappsilber J. (2019). Co-regulation map of the human proteome enables identification of protein functions. Nat Biotechnol 37, 1361–1371. [PubMed: 31690884]

Li J, Li J, Zhao WG, Sun HD, Guo ZG, Liu XY, Tang XY, She ZF, Yuan T, Liu SN, et al. (2020a). Comprehensive proteomics and functional annotation of mouse brown adipose tissue. PLoS One 15, e0232084.

Li J, Paulo JA, Nusinow DP, Huttlin EL, and Gygi SP (2019). Investigation of Proteomic and Phosphoproteomic Responses to Signaling Network Perturbations Reveals Functional Pathway Organizations in Yeast. Cell Rep 29, 2092–2104 e2094. [PubMed: 31722220]

Li J, Van Vranken JG, Pontano Vaites L, Schweppe DK, Huttlin EL, Etienne C, Nandhikonda P, Viner R, Robitaille AM, Thompson AH, et al. (2020b). TMTpro reagents: a set of isobaric labeling mass tags enables simultaneous proteome-wide measurements across 16 samples. Nat Methods 17, 399–404. [PubMed: 32203386]

Lodhi IJ, Yin L, Jensen-Urstad APL, Funai K, Coleman T, Baird JH, El Ramahi MK, Razani B, Song HW, Fong FH, et al. (2012). Inhibiting Adipose Tissue Lipogenesis Reprograms Thermogenesis and PPAR gamma Activation to Decrease Diet-Induced Obesity. Cell Metabolism 16, 189–201. [PubMed: 22863804]

Logan RW, Robledo RF, Recla JM, Philip VM, Bubier JA, Jay JJ, Harwood C, Wilcox T, Gatti DM, Bult CJ, et al. (2013). High-precision genetic mapping of behavioral traits in the diversity outbred mouse population. Genes Brain Behav 12, 424–437. [PubMed: 23433259]

Martens JH, and Stunnenberg HG (2013). BLUEPRINT: mapping human blood cell epigenomes. Haematologica 98, 1487–1489. [PubMed: 24091925]

McAlister GC, Nusinow DP, Jedrychowski MP, Wuhr M, Huttlin EL, Erickson BK, Rad R, Haas W, and Gygi SP (2014). MultiNotch MS3 Enables Accurate, Sensitive, and Multiplexed Detection of Differential Expression across Cancer Cell Line Proteomes. Analytical Chemistry 86, 7150–7158. [PubMed: 24927332]

Mills EL, Pierce KA, Jedrychowski MP, Garrity R, Winther S, Vidoni S, Yoneshiro T, Spinelli JB, Lu GZ, Kazak L, et al. (2018). Accumulation of succinate controls activation of adipose tissue thermogenesis. Nature 560, 102-+.

Muller S, Balaz M, Stefanicka P, Varga L, Amri EZ, Ukropec J, Wollscheid B, and Wolfrum C. (2016). Proteomic Analysis of Human Brown Adipose Tissue Reveals Utilization of Coupled and Uncoupled Energy Expenditure Pathways. Sci Rep 6, 30030.

Navarrete-Pere J., Y Q., Gyg SP., and Paul JA. (2018). Streamlined Tandem Mass Tag (SL-TMT) Protocol: An Efficient Strategy for Quantitative (Phospho)proteome Profiling Using Tandem Mass Tag-Synchronous Precursor Selection-MS3. J Proteome Res 17, 2226–2236. [PubMed: 29734811]

Nedergaard J, Bengtsson T, and Cannon B. (2007). Unexpected evidence for active brown adipose tissue in adult humans. Am J Physiol Endocrinol Metab 293, E444–452. [PubMed: 17473055]

Newman AM, Steen CB, Liu CL, Gentles AJ, Chaudhuri AA, Scherer F, Khodadoust MS, Esfahani MS, Luca BA, Steiner D, et al. (2019). Determining cell type abundance and expression from bulk tissues with digital cytometry. Nat Biotechnol 37, 773–782. [PubMed: 31061481]

Nusinow DP, and Gygi SP (2020). A Guide to the Quantitative Proteomic Profiles of the Cancer Cell Line Encyclopedia. bioRxiv, 2020.2002.2003.932384.

Nusinow DP, Szpyt J, Ghandi M, Rose CM, McDonald ER 3rd, Kalocsay M, Jane-Valbuena J, Gelfand E, Schweppe DK, Jedrychowski M, et al. (2020). Quantitative Proteomics of the Cancer Cell Line Encyclopedia. Cell 180, 387–402 e316. [PubMed: 31978347]

Oughtred R, Stark C, Breitkreutz BJ, Rust J, Boucher L, Chang C, Kolas N, O'Donnell L, Leung G, McAdam R, et al. (2019). The BioGRID interaction database: 2019 update. Nucleic Acids Res 47, D529–D541. [PubMed: 30476227]

Peng JM, Elias JE, Thoreen CC, Licklider LJ, and Gygi SP (2003). Evaluation of multidimensional chromatography coupled with tandem mass spectrometry (LC/LC-MS/MS) for large-scale protein analysis: The yeast proteome. Journal of Proteome Research 2, 43–50. [PubMed: 12643542]

Perdikari A, Leparc GG, Balaz M, Pires ND, Lidell ME, Sun W, Fernandez-Albert F, Muller S, Akchiche N, Dong H, et al. (2018). BATLAS: Deconvoluting Brown Adipose Tissue. Cell Rep 25, 784–797 e784. [PubMed: 30332656]

Perez-Riverol Y, Csordas A, Bai JW, Bernal-Llinares M, Hewapathirana S, Kundu DJ, Inuganti A, Griss J, Mayer G, Eisenacher M, et al. (2019). The PRIDE database and related tools and resources in 2019: improving support for quantification data. Nucleic Acids Research 47, D442–D450. [PubMed: 30395289]

Pinero J, Ramirez-Anguita JM, Sauch-Pitarch J, Ronzano F, Centeno E, Sanz F, and Furlong LI (2020). The DisGeNET knowledge platform for disease genomics: 2019 update. Nucleic Acids Res 48, D845–D855. [PubMed: 31680165]

Pinero J, Sauch J, Sanz F, and Furlong LI (2021). The DisGeNET cytoscape app: Exploring and visualizing disease genomics data. Comput Struct Biotechnol J 19, 2960–2967. [PubMed: 34136095]

Rahbani JF, Roesler A, Hussain MF, Samborska B, Dykstra CB, Tsai L, Jedrychowski MP, Vergnes L, Reue K, Spiegelman BM, et al. (2021). Creatine kinase B controls futile creatine cycling in thermogenic fat. Nature 590, 480–485. [PubMed: 33597756]

Rajakumari S, Wu J, Ishibashi J, Lim HW, Giang AH, Won KJ, Reed RR, and Seale P. (2013). EBF2 Determines and Maintains Brown Adipocyte Identity. Cell Metabolism 17, 562–574. [PubMed: 23499423]

Rath S, Sharma R, Gupta R, Ast T, Chan C, Durham TJ, Goodman RP, Grabarek Z, Haas ME, Hung WHW, et al. (2021). MitoCarta3.0: an updated mitochondrial proteome now with sub-organelle localization and pathway annotations. Nucleic Acids Res 49, D1541–D1547. [PubMed: 33174596]

Recla JM, Robledo RF, Gatti DM, Bult CJ, Churchill GA, and Chesler EJ (2014). Precise genetic mapping and integrative bioinformatics in Diversity Outbred mice reveals Hydin as a novel pain gene. Mamm Genome 25, 211–222. [PubMed: 24700285]

Reddy A, Bozi LHM, Yaghi OK, Mills EL, Xiao H, Nicholson HE, Paschini M, Paulo JA, Garrity R, Laznik-Bogoslavski D, et al. (2020). pH-Gated Succinate Secretion Regulates Muscle Remodeling in Response to Exercise. Cell 183, 62–75 e17. [PubMed: 32946811]

Rockman MV, and Kruglyak L. (2006). Genetics of global gene expression. Nat Rev Genet 7, 862–872. [PubMed: 17047685]

Roh HC, Tsai LTY, Shao M, Tenen D, Shen Y, Kumari M, Lyubetskaya A, Jacobs C, Dawes B, Gupta RK, et al. (2018). Warming Induces Significant Reprogramming of Beige, but Not Brown, Adipocyte Cellular Identity. Cell Metab 27, 1121–1137 e1125. [PubMed: 29657031]

Romanov N, Kuhn M, Aebersold R, Ori A, Beck M, and Bork P. (2019). Disentangling Genetic and Environmental Effects on the Proteotypes of Individuals. Cell 177, 1308-+.

Rosen ED, and Spiegelman BM (2014). What we talk about when we talk about fat. Cell 156, 20–44. [PubMed: 24439368]

Ruepp A, Waegele B, Lechner M, Brauner B, Dunger-Kaltenbach I, Fobo G, Frishman G, Montrone C, and Mewes HW (2010). CORUM: the comprehensive resource of mammalian protein complexes−-2009. Nucleic Acids Res 38, D497–501. [PubMed: 19884131]

Saul MC, Philip VM, Reinholdt LG, Center for Systems Neurogenetics of, A., and Chesler EJ (2019). High-Diversity Mouse Populations for Complex Traits. Trends Genet 35, 501–514. [PubMed: 31133439]

Savitski MM, Wilhelm M, Hahne H, Kuster B, and Bantscheff M. (2015). A Scalable Approach for Protein False Discovery Rate Estimation in Large Proteomic Data Sets. Mol Cell Proteomics 14, 2394–2404. [PubMed: 25987413]

Schindelin J, Arganda-Carreras I, Frise E, Kaynig V, Longair M, Pietzsch T, Preibisch S, Rueden C, Saalfeld S, Schmid B, et al. (2012). Fiji: an open-source platform for biological-image analysis. Nat Methods 9, 676–682. [PubMed: 22743772]

Schneider CA, Rasband WS, and Eliceiri KW (2012). NIH Image to ImageJ: 25 years of image analysis. Nature Methods 9, 671–675. [PubMed: 22930834]

Schweppe DK., Prasad S., Belford MW., Navarrete-Perea J., Bailey DJ., Huguet R., Jedrychowski MP., Rad R., McAlister G., Abbatiell SE., et al. . (2019). Characterization and Optimization of Multiplexed Quantitative Analyses Using High-Field Asymmetric-Waveform Ion Mobility Mass Spectrometry. Anal Chem 91, 4010–4016. [PubMed: 30672687]

Schweppe DK, Rusin SF, Gygi SP, and Paulo JA (2020). Optimized Workflow for Multiplexed Phosphorylation Analysis of TMT-Labeled Peptides Using High-Field Asymmetric Waveform Ion Mobility Spectrometry. Journal of Proteome Research 19, 554–560. [PubMed: 31799850]

Shabalina IG, Petrovic N, de Jong JM, Kalinovich AV, Cannon B, and Nedergaard J. (2013). UCP1 in brite/beige adipose tissue mitochondria is functionally thermogenic. Cell Rep 5, 1196–1203. [PubMed: 24290753]

Shabalina IG, Vrbacky M, Pecinova A, Kalinovich AV, Drahota Z, Houstek J, Mracek T, Cannon B, and Nedergaard J. (2014). ROS production in brown adipose tissue mitochondria: the question of UCP1-dependence. Biochim Biophys Acta 1837, 2017–2030. [PubMed: 24769119]

Shannon P, Markiel A, Ozier O, Baliga NS, Wang JT, Ramage D, Amin N, Schwikowski B, and Ideker T. (2003). Cytoscape: A software environment for integrated models of biomolecular interaction networks. Genome Res 13, 2498–2504. [PubMed: 14597658]

Shinoda K, Luijten IH, Hasegawa Y, Hong H, Sonne SB, Kim M, Xue R, Chondronikola M, Cypess AM, Tseng YH, et al. (2015). Genetic and functional characterization of clonally derived adult human brown adipocytes. Nat Med 21, 389–394. [PubMed: 25774848]

Simon MM, Greenaway S, White JK, Fuchs H, Gailus-Durner V, Wells S, Sorg T, Wong K, Bedu E, Cartwright EJ, et al. (2013). A comparative phenotypic and genomic analysis of C57BL/6J and C57BL/6N mouse strains. Genome Biol 14, R82. [PubMed: 23902802]

Smith FD, Samelson BK, and Scott JD (2011). Discovery of cellular substrates for protein kinase A using a peptide array screening protocol. Biochem J 438, 103–110. [PubMed: 21644927]

Snyder MM, Yue F, Zhang L, Shang R, Qiu J, Chen J, Kim KH, Peng Y, Oprescu SN, Donkin SS, et al. (2021). LETMD1 is required for mitochondrial structure and thermogenic function of brown adipocytes. FASEB J 35, e21965.

Speliotes EK, Willer CJ, Berndt SI, Monda KL, Thorleifsson G, Jackson AU, Allen HL, Lindgren CM, Luan J, Magi R, et al. (2010). Association analyses of 249,796 individuals reveal 18 new loci associated with body mass index. Nat Genet 42, 937–U953. [PubMed: 20935630]

Staals RH, Bronkhorst AW, Schilders G, Slomovic S, Schuster G, Heck AJ, Raijmakers R, and Pruijn GJ (2010). Dis3-like 1: a novel exoribonuclease associated with the human exosome. EMBO J 29, 2358–2367. [PubMed: 20531389]

Stalder L, Banaei-Esfahani A, Ciuffa R, Payne JL, and Aebersold R. (2020). SWATH-MS co-expression profiles reveal paralogue interference in protein complex evolution. bioRxiv, 2020.2009.2008.287334.

Strimmer K. (2008a). fdrtool: a versatile R package for estimating local and tail area-based false discovery rates. Bioinformatics 24, 1461–1462. [PubMed: 18441000]

Strimmer K. (2008b). A unified approach to false discovery rate estimation. BMC Bioinformatics 9, 303. [PubMed: 18613966]

Sun W, Dong H, Balaz M, Slyper M, Drokhlyansky E, Colleluori G, Giordano A, Kovanicova Z, Stefanicka P, Balazova L, et al. (2020). snRNA-seq reveals a subpopulation of adipocytes that regulates thermogenesis. Nature 587, 98–102. [PubMed: 33116305]

Sun XJ, Rothenberg P, Kahn CR, Backer JM, Araki E, Wilden PA, Cahill DA, Goldstein BJ, and White MF (1991). Structure of the Insulin-Receptor Substrate Irs-1 Defines a Unique Signal Transduction Protein. Nature 352, 73–77. [PubMed: 1648180]

Sun Y, Rahbani JF, Jedrychowski MP, Riley CL, Vidoni S, Bogoslavski D, Hu B, Dumesic PA, Zeng X, Wang AB, et al. (2021). Mitochondrial TNAP controls thermogenesis by hydrolysis of phosphocreatine. Nature 593, 580–585. [PubMed: 33981039]

Szklarczyk D, Morris JH, Cook H, Kuhn M, Wyder S, Simonovic M, Santos A, Doncheva NT, Roth A, Bork P, et al. (2017). The STRING database in 2017: quality-controlled protein-protein association networks, made broadly accessible. Nucleic Acids Res 45, D362–D368. [PubMed: 27924014]

Thul PJ, Akesson L, Wiking M, Mahdessian D, Geladaki A, Ait Blal H, Alm T, Asplund A, Bjork L, Breckels LM, et al. (2017). A subcellular map of the human proteome. Science 356.

Tibshiran R. (1996). Regression shrinkage and selection via the Lasso. J Roy Stat Soc B Met 58, 267–288.

Tifoun N, De Las Heras JM, Guillaume A, Bouleau S, Mignotte B, and Le Floch N. (2021). Insights into the Roles of the Sideroflexins/SLC56 Family in Iron Homeostasis and Iron-Sulfur Biogenesis. Biomedicines 9.

Uhlen M, Fagerberg L, Hallstrom BM, Lindskog C, Oksvold P, Mardinoglu A, Sivertsson A, Kampf C, Sjostedt E, Asplund A, et al. (2015). Proteomics. Tissue-based map of the human proteome. Science 347, 1260419.

UniProt C. (2021). UniProt: the universal protein knowledgebase in 2021. Nucleic Acids Res 49, D480–D489. [PubMed: 33237286]

Valdar W, Holmes CC, Mott R, and Flint J. (2009). Mapping in structured populations by resample model averaging. Genetics 182, 1263–1277. [PubMed: 19474203]

Wang M, Weiss M, Simonovic M, Haertinger G, Schrimpf SP, Hengartner MO, and von Mering C. (2012). PaxDb, a database of protein abundance averages across all three domains of life. Mol Cell Proteomics 11, 492–500. [PubMed: 22535208]

Wang W, and Seale P. (2016). Control of brown and beige fat development. Nat Rev Mol Cell Biol 17, 691–702. [PubMed: 27552974]

Welsh CE, and McMillan L. (2012). Accelerating the inbreeding of multi-parental recombinant inbred lines generated by sibling matings. G3 (Bethesda) 2, 191–198. [PubMed: 22384397]

Wessel D, and Flugge UI (1984). A Method for the Quantitative Recovery of Protein in Dilute-Solution in the Presence of Detergents and Lipids. Anal Biochem 138, 141–143. [PubMed: 6731838]

Wickham H, Averick M, Bryan J, Chang W, McGowan LDA, François R, Grolemund G, Hayes A, Henry L, and Hester J. (2019). Welcome to the Tidyverse. Journal of open source software 4, 1686.

Williams EG, Wu Y, Wolski W, Kim JY, Lan J, Hasan M, Halter C, Jha P, Ryu D, Auwerx J, et al. (2018). Quantifying and Localizing the Mitochondrial Proteome Across Five Tissues in A Mouse Population. Mol Cell Proteomics 17, 1766–1777. [PubMed: 29945935]

Wu W, Shi F, Liu D, Ceddia RP, Gaffin R, Wei W, Fang H, Lewandowski ED, and Collins S. (2017). Enhancing natriuretic peptide signaling in adipose tissue, but not in muscle, protects against diet-induced obesity and insulin resistance. Sci Signal 10.

Xiao HP, Jedrychowski MP, Schweppe DK, Huttlin EL, Yu Q, Heppner DE, Li JM, Long JN, Mills EL, Szpyt J, et al. (2020). A Quantitative Tissue-Specific Landscape of Protein Redox Regulation during Aging. Cell 180, 968-+.

Yang H, Wang JR, Didion JP, Buus RJ, Bell TA, Welsh CE, Bonhomme F, Yu AH, Nachman MW, Pialek J, et al. (2011). Subspecific origin and haplotype diversity in the laboratory mouse. Nat Genet 43, 648–655. [PubMed: 21623374]

Yates AD, Achuthan P, Akanni W, Allen J, Allen J, Alvarez-Jarreta J, Amode MR, Armean IM, Azov AG, Bennett R, et al. (2020). Ensembl 2020. Nucleic Acids Res 48, D682–D688. [PubMed: 31691826]

Yoneshiro T, Wang Q, Tajima K, Matsushita M, Maki H, Igarashi K, Dai Z, White PJ, McGarrah RW, Ilkayeva OR, et al. (2019). BCAA catabolism in brown fat controls energy homeostasis through SLC25A44. Nature 572, 614–619. [PubMed: 31435015]

Yu Q., Xiao H., Jedrychowski MP., Schweppe DK., Navarrete-Perea J., Knott J., Rogers J., Chouchani ET., and Gygi SP. (2020). Sample multiplexing for targeted pathway proteomics in aging mice. Proc Natl Acad Sci U S A 117, 9723–9732. [PubMed: 32332170]

Zeng X, Ye M, Resch JM, Jedrychowski MP, Hu B, Lowell BB, Ginty DD, and Spiegelman BM (2019). Innervation of thermogenic adipose tissue via a calsyntenin 3beta-S100b axis. Nature 569, 229–235. [PubMed: 31043739]

Zhang Y, Proenca R, Maffei M, Barone M, Leopold L, and Friedman JM (1994). Positional cloning of the mouse obese gene and its human homologue. Nature 372, 425–432. [PubMed: 7984236]

Highlights

- Diversity outbred proteome architecture annotates biological function of BAT proteins
- Co-operative network analysis reveals novel regulators of metabolic physiology
- QTL analysis to guide strain selection for specific phenotypic outcomes
- Uncovering SFXN5, LETMD1, and ATP1A2 as modulators of BAT thermogenesis and adiposity

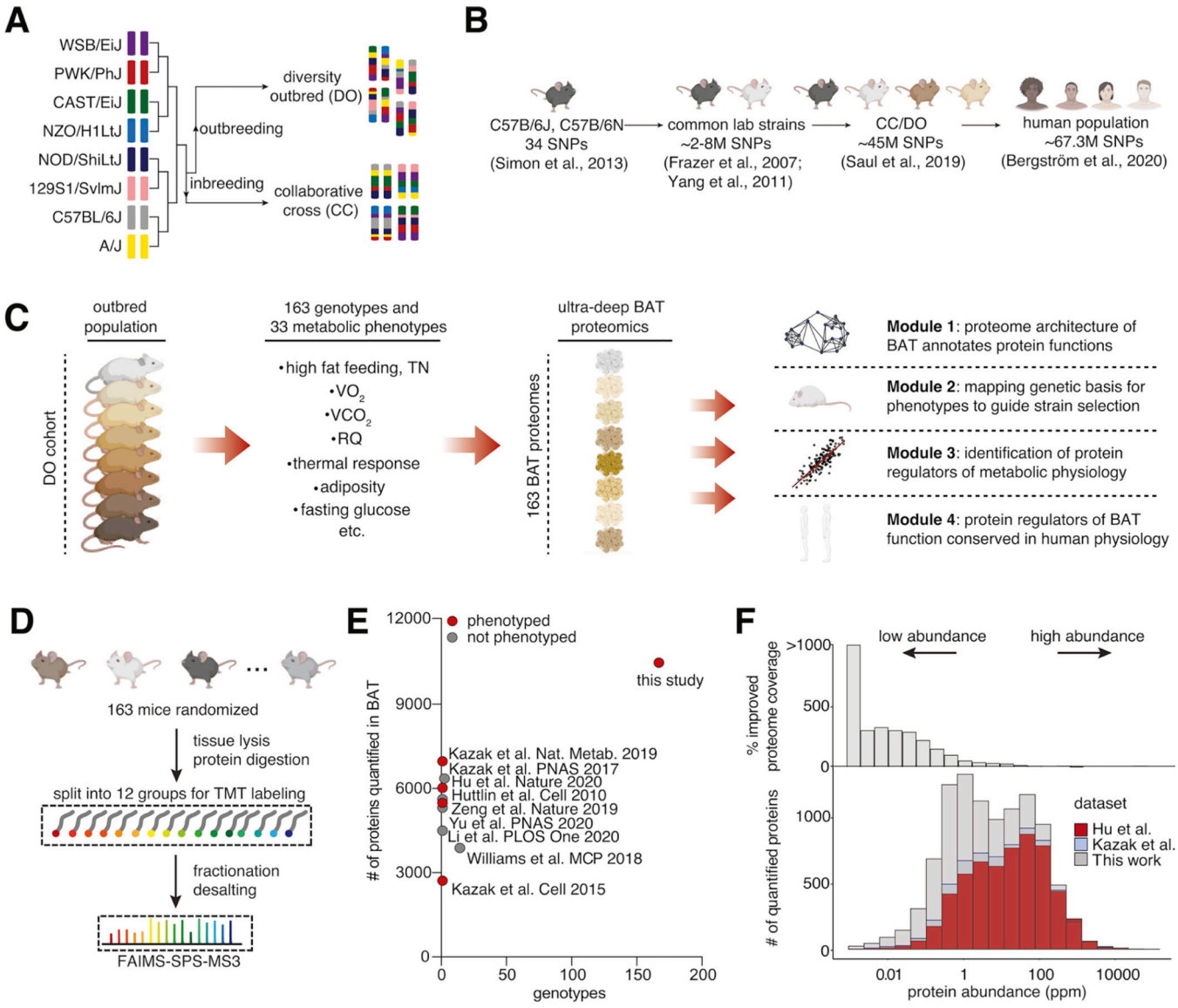

Figure 1: Measuring genotypes, phenotypes, and proteomes in the DO cohort

(A) Overview of the breeding scheme for the collaborative cross (CC) and diversity outbred (DO) strains.

(B) Comparison of single nucleotide polymorphisms (SNPs) across various populations.

(C) Experimental design of OPABAT.

(D) TMT-based BAT protein quantification.

(E) Genotype and proteome coverage of OPABAT compared to other studies.

(F) OPABAT quantifies more low-abundance proteins than previous reports.

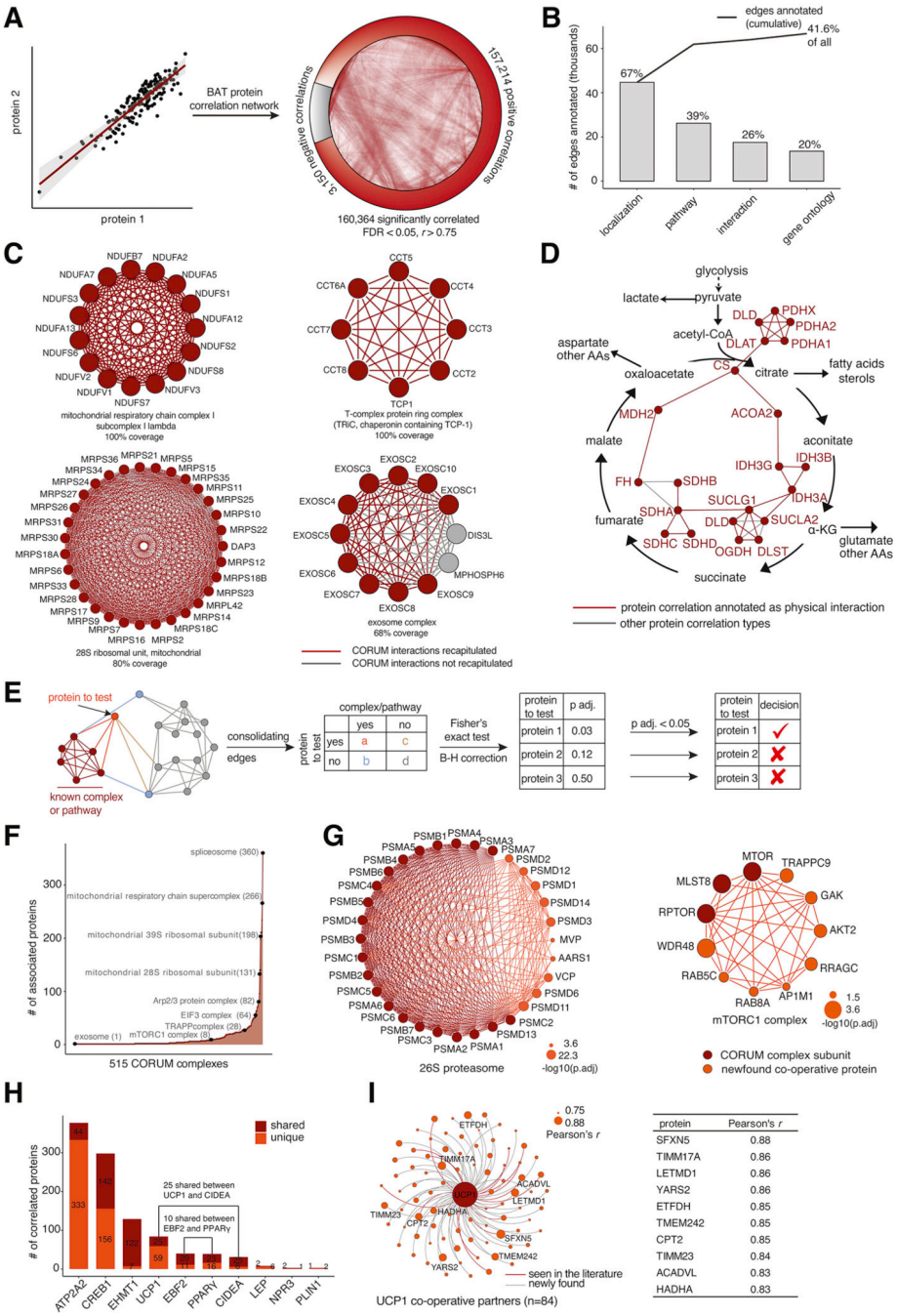

Figure 2: Co-variation analysis identifies co-operative proteins

(A) OPABAT co-expression network.

(B) Co-operative edges in OPABAT explained by literature evidence.

(C) Highly recapitulated CORUM complexes in OPABAT. Red nodes-recapitulated network members; gray nodes-missing network members

(D) OPABAT edges recapitulated the TCA cycle.

(E) Determining co-operative proteins of known protein complexes or pathways. Red nodes-known members of established networks; blue nodes-neighboring proteins; orange node-the protein to test co-operativity; gray nodes-all other proteins in OPABAT.
(F) CORUM core complexes and co-operative proteins.
(G) Exemplary co-operative proteins of established complexes. Red edges-interactions between complex subunits; orange edges-interactions involving co-operative proteins.
(H) Co-operative proteins of established regulators of thermogenesis.
(I) Co-operative partners of UCP1. Red edges- co-operative proteins with evidence in the literature; gray edges- no evidence in the literature; table-top 10 co-operative proteins of UCP1.

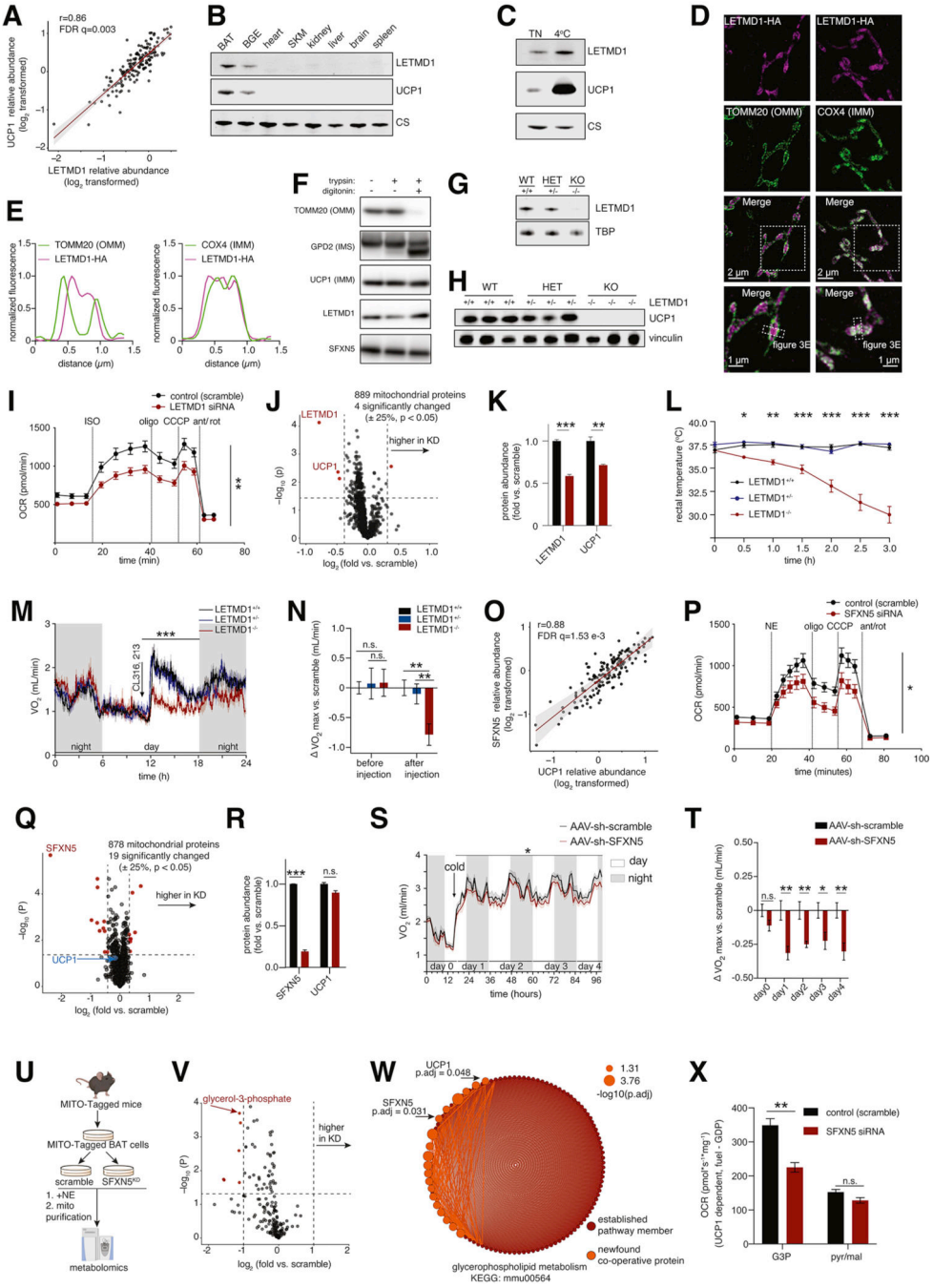

Figure 3: OPABAT identifies LETMD1 and SFXN5 as regulators of UCP1-dependent BAT thermogenesis

(A) LETMD1expression highly correlated with UCP1.

(B) LETMD1 and UCP1 shared similar mitochondrial expression profiles in tissues. BGE-beige fat; SKM- skeletal muscle.

(C) Cold-inducible LETMD1 and UCP1 expression in BAT.

(D) Structured illumination microscopy (SIM) of LETMD1-HA (purple) with mitochondria outer membrane (OMM) marker TOMM20 (green) and inner outer membrane (IMM) COX4 (green). 60 X magnification.

(E) LETMD1-HA fluorescence signal co-localized with COX4 but not TOM20.

(F) Trypsin digestion assay of UCP1, LETMD1, and SFXN5 along with TOMM22 (OMM) and GPD2 (intermembrane space, IMS).

(G) BAT LETMD1 expression in wildtype (WT, $LETMD^{+/+}$), heterozygous (HET, $LETMD^{+/-}$), and full knockout (KO, $LETMD^{-/-}$) C57BL/6J mice.

(H) BAT UCP1 expression in LETMD1 WT, HET, and KO mice. n = 3.

(I) LETMD1 knockdown (KD) attenuated cellular respiration in differentiated brown adipocytes. OCR-oxygen consumption rate; ISO-isoproterenol; oligo-oligomycin; CCCP-carbonyl cyanide 3-chlorophenylhydrazone; ant/rot-antimycin/rotenone. n = 10.

(J)-(K) LETMD1 KD specifically decreased UCP1 abundance. n=3.

(L) $LETMD^{-/-}$ mice could not maintain body temperature when exposed to cold (4 ^{o}C). WT, n = 3; HET, n = 4; KO, n = 5.

(M)-(N) $LETMD^{-/-}$ mice had blunted response in respiration to CL316, 213 injection. Baseline measured at thermoneutrality. WT, n = 8; HET, n = 6; KO, n = 5.

(O) SFXN5-UCP1 abundance correlation.

(P) SFXN5 KD attenuated cellular respiration in differentiated brown adipocytes. OCR-oxygen consumption rate; NE-norepinephrine; oligo-oligomycin; CCCP-carbonyl cyanide 3-chlorophenylhydrazone; ant/rot-antimycin/rotenone. n = 10.

(Q)-(R) SFXN5 KD did not change UCP1 abundance. n=3.

(S)-(T) $SFXN5^{KD}$ mice have blunted response in respiration to cold exposure. Baseline-room temperature. n=6.

(U)-(V) MITO-Tag-based metabolomics identified G3P depletion in the mitochondria of $SFXN5^{KD}$ cells with NE treatment. WT, n=4; KD, n=6.

(W) SFXN5 and UCP1 are newfound co-operative proteins of the KEGG glycerophospholipid metabolism pathway in OPABAT. Red nodes and edges- established pathway; orange nodes and edges- new co-operative proteins/edges.

(X) UCP1-dependent respiration in WT and $SFXN5^{KD}$ mature brown adipocyte mitochondria using different fuel source, calculated by OCR of G3P (or pyruvate/malate) - OCR of GDP. n=3.

Data presented as mean ± S.E.M. * $p < 0.05$, ** $p< 0.01$, *** $p<0.001$. (I), (L), (M), (P), and (S), two-way ANOVA test. (J), (K), (N), (Q), (R), (T), (V), and (X), two-tailed Student's t test. (W), Fisher's exact test.

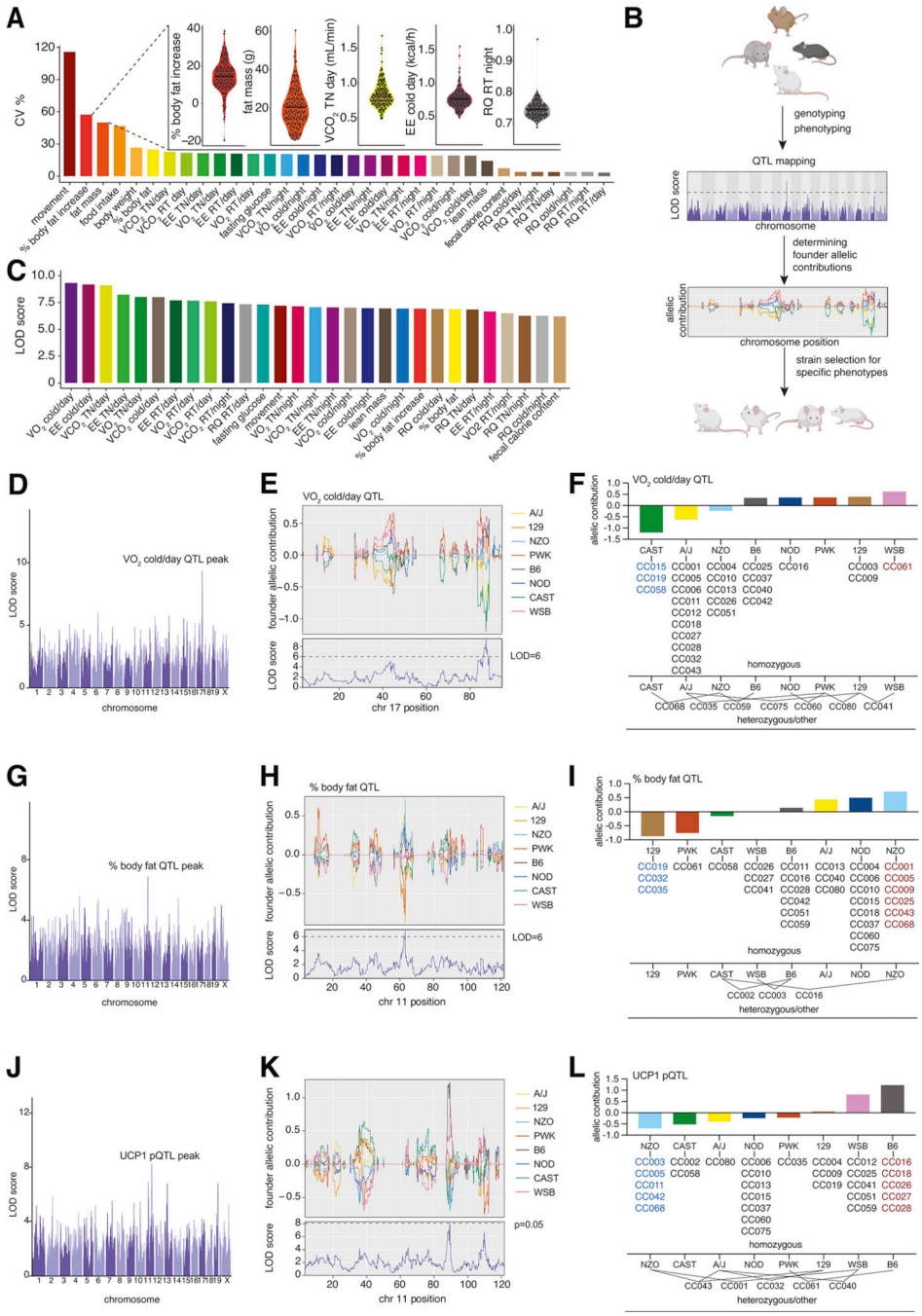

Figure 4: Genetic basis for phenotypic variation

(A) Variability of metabolic parameters in the DO cohort.

(B) Workflow of QTL mapping and mouse strain selection.

(C) Phenotype QTLs with LOD score > 6 (the presence of a QTL is 10^6 times more probable than its absence).

(D) Manhattan plot of the VO_2 cold/day QTL.

(E) Founder strain allelic contribution to VO_2 cold/day (QTL- chromosome 17, 87.49Mbp).

(F) Founder and CC strain selection for low (blue) or high (red) VO_2 cold/day.

(G) Manhattan plot of the % body fat QTL.

(H) Founder strain allelic contribution to % body fat (QTL- chromosome 11, 63.08 Mbp).

(I) Founder and CC strain selection for low (blue) or high (red) % body fat.

(J) Manhattan plot of the UCP1 pQTL.

(K) Founder strain allelic contribution to UCP1 protein abundance. (QTL- chromosome 11, 89.47 Mbp). P value obtained from permutation test with 10,000 iterations.

(L) Founder and CC strain selection for low (blue) or high (red) UCP1 protein expression.

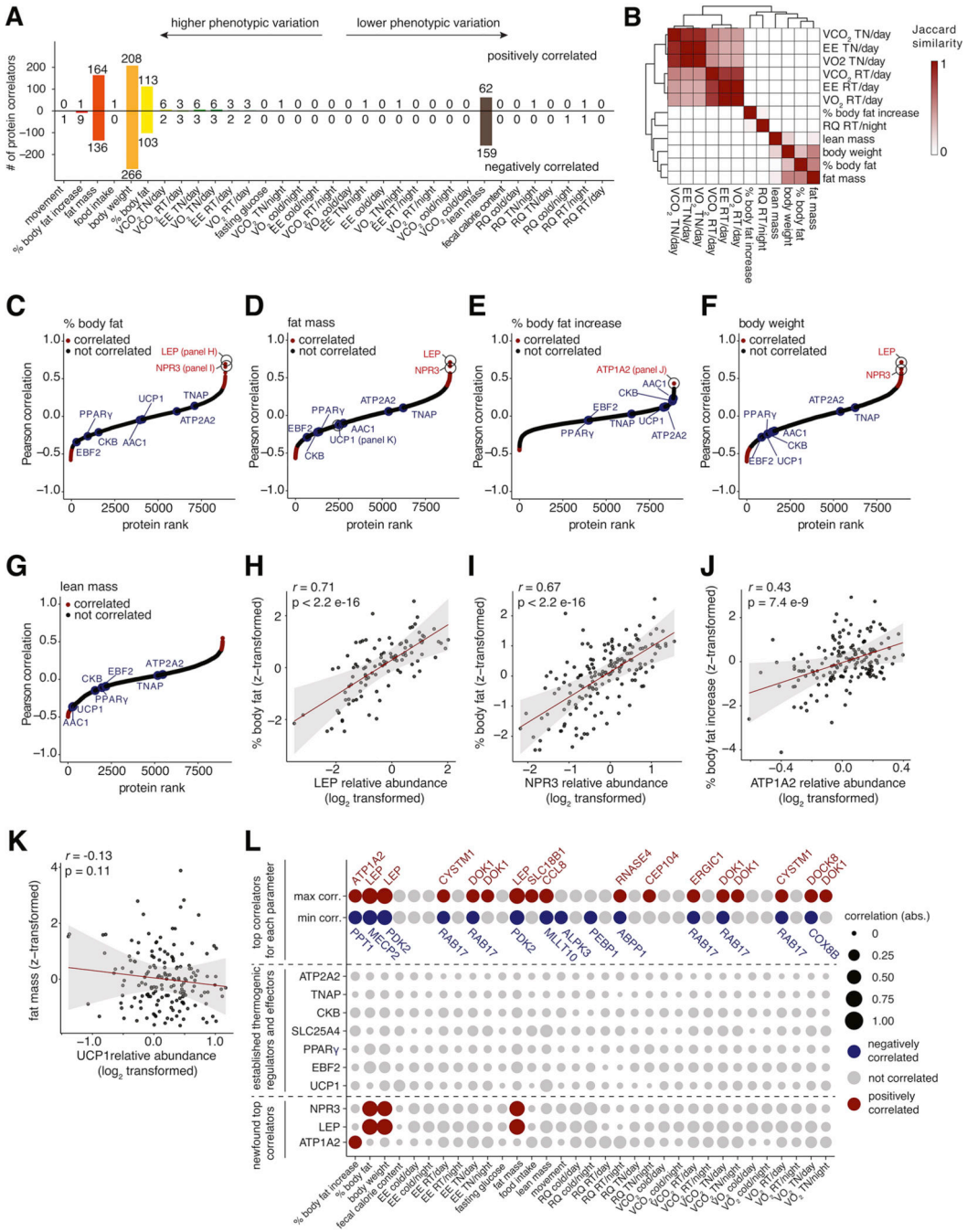

Figure 5: BAT protein determinants of whole-body metabolic physiology

(A) Number of significant positive and negative protein correlators of each parameter.

(B) Jaccard similarity of protein correlators between metabolic parameters.

(C)-(G) OPABAT protein correlators of adiposity parameters.

(H) Correlation between LEP abundance and % body fat.

(I) Correlation between NPR3 abundance and % body fat.

(J) Correlation between ATP1A2 abundance and % body fat increase.

(K) Correlation between UCP1 abundance and fat mass.

(L) Correlation between all metabolic phenotypes and top protein correlators/major established BAT regulators of thermogenesis.

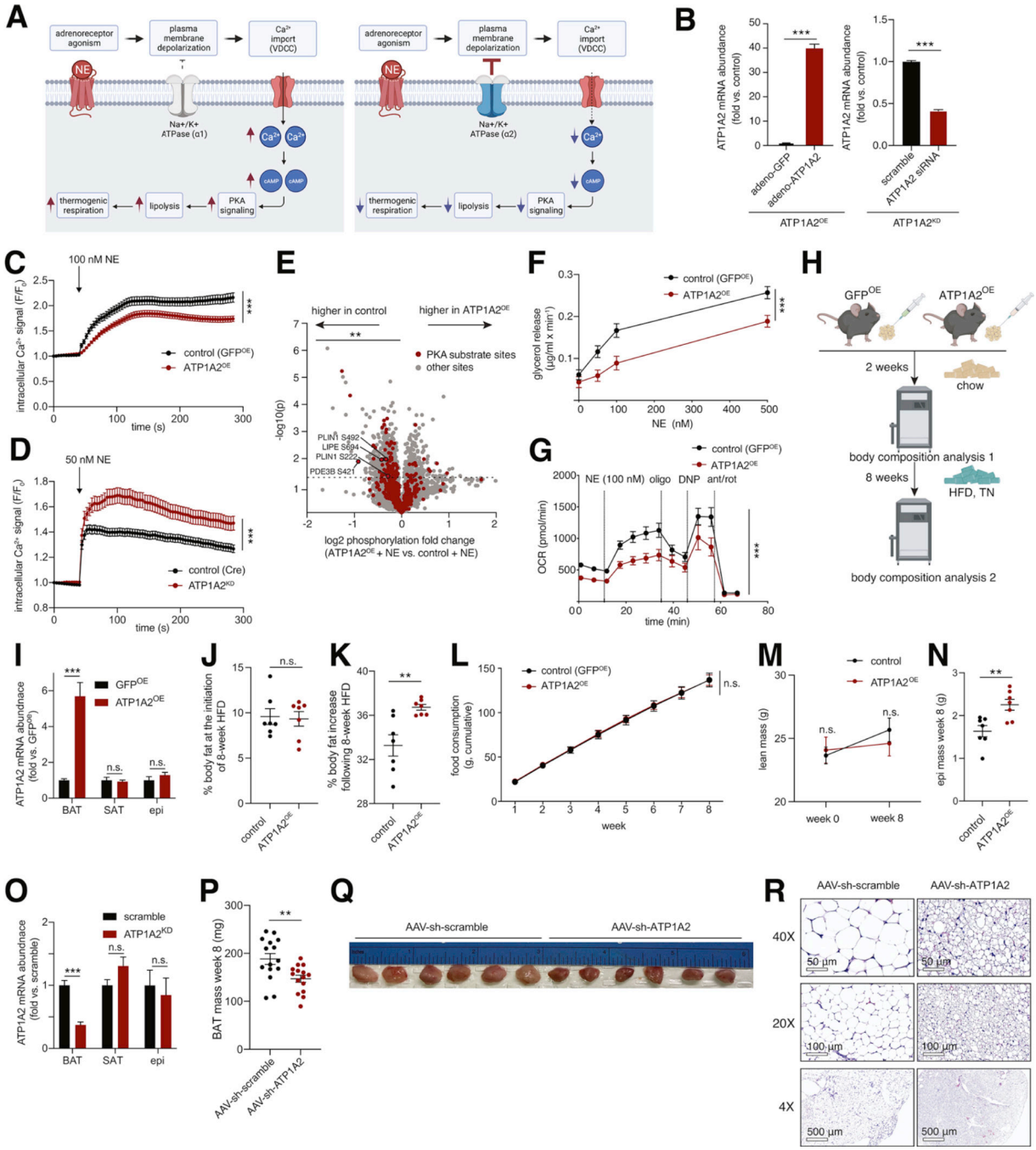

Figure 6: ATP1A2 inhibits BAT energy expenditure

(A) A model of ATP1A2 as a negative regulator of BAT energy expenditure.

(B) Generation of ATP1A2 overexpression ($ATP1A2^{OE}$) and ATP1A2 knockdown ($ATP1A2^{KD}$) brown adipocytes with adenovirus or siRNA. n = 3.

(C) Averaged Fluo-4 intensity trace (normalized to intensity at 0 min) of control and $ATP1A2^{OE}$ differentiated brown adipocytes. Intensity plotted as the relative change to baseline-F/F_0. n = 209 cells.

(D) Averaged Fluo-4 intensity trace (normalized to intensity at 0 min) of control and ATP1A2^{KD} differentiated brown adipocytes. Intensity plotted as the relative change to baseline-F/F_0. n = 209 cells.
(E) Downregulation of PKA substrate phosphorylation in ATP1A2^{OE} differentiated brown adipocytes compared to GFP control measured by phosphoproteomics. n = 4.
(F) ATP1A2 OE attenuated lipolysis in differentiated brown adipocytes. n = 4.
(G) ATP1A2 OE attenuated cellular respiration in differentiated brown adipocytes. OCR-Oxygen consumption rate; NE-norepinephrine; oligo-oligomycin; DNP- 2,4-Dinitrophenol; ant/rot-antimycin/rotenone. n = 4.
(H) Body composition analysis of control and BAT-specific ATP1A2^{OE} mice under HFD and TN.
(I) qPCR analysis of ATP1A2 OE in BAT, SAT, and epididymal fat (epi) 2 weeks post injection. n=8.
(J) % body fat of ATP1A2^{KD} and control cohorts at the initiation of HFD. n = 7.
(K) ATP1A2^{OE} and control cohorts % body fat increase post HFD. n = 7.
(L) ATP1A2^{OE} and control cohorts food consumption under HFD. n = 7.
(M) ATP1A2^{OE} and control cohorts lean mass under HFD. n = 7.
(N) ATP1A2^{OE} and control cohorts epi mass post HFD. n = 7.
(O) qPCR analysis of ATP1A2 KD in BAT, SAT, and epi. n=4.
(P) BAT mass of ATP1A2^{KD} and control cohorts post HFD. n = 15.
(Q) BAT tissue appearance post HFD.
(R) BAT histology with H&E staining. The ATP1A2^{KD} BAT exhibited presence of many small lipid droplets and less whitening. n=3.
Data presented as mean ± S.E.M. * $p < 0.05$, ** $p< 0.01$, *** $p<0.001$. (B), (E- fold change), (I), (J), (K),
(M), (N), (O), (P), two-tailed Student’s t test; (E-association), Fisher’s exact test; (C), (D), (F), (G), (L), two-way ANOVA test.

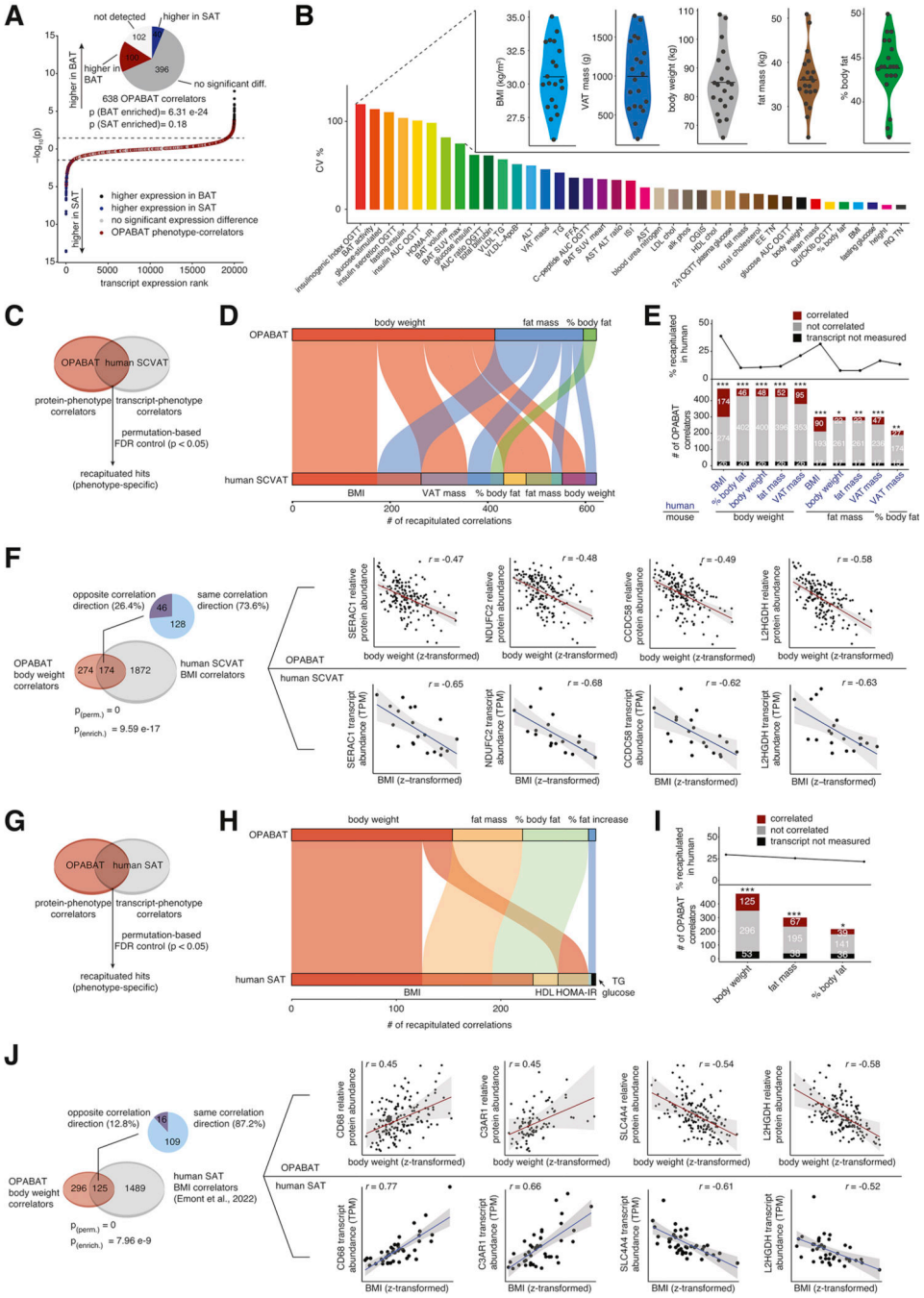

Figure 7: Human relevance of OPABAT metabolic physiology correlators

(A) OPABAT correlators are enriched among transcripts with higher BAT expression than SAT in human. n=10.

(B) Variability of metabolic parameters in a cohort of 20 female patients.

(C) Comparing OPABAT protein-phenotype correlators to human SCVAT transcript-phenotype correlators.

(D) Recapitulated correlators of adiposity between OPABAT and human SCVAT.

(E) Number and percentage of adiposity correlators recapitulated in human SCVAT.

(F) OPABAT correlators of body weight recapitulated as human SCVAT correlators of BMI.
(G) Comparing OPABAT protein-phenotype correlators to human SAT transcript-phenotype correlators.
(H) Recapitulated correlators of adiposity between OPABAT and human SAT.
(I) Number and percentage of adiposity correlators recapitulated in human SAT.
(J) OPABAT correlators of body weight recapitulated as human SAT correlators of BMI.
* $p < 0.05$, ** $p < 0.01$, *** $p<0.001$. (E), (F), (I), and (J) permutation test. (A), (F and J-enrichment), Fisher's exact test.

KEY RESOURCES TABLE

REAGENT or RESOURCE	SOURCE	IDENTIFIER
Antibodies		
Anti-HA mouse mAb	Abcam	Cat#ab18181, RRID:AB_444303
Anti-Rabbit IgG HRP Conjugate	Promega	Cat#W4011, RRID:AB_430833
IRDye secondary antibody	LICOR	Cat#925-68071, RRID:AB_2721181
Anti-TOMM20 rabbit mAb	Cell Signaling	Cat#42406, RRID:AB_2687663
Anti-COX4 rabbit mAb	Cell Signaling	Cat#4850, RRID:AB_ 2085424
Anti-mouse Alexa Fluor 568	Invitrogen	Cat#A-11004, RRID:AB_2534072
Anti-rabbit Alexa Fluor 647	Invitrogen	Cat#A-21245, RRID:AB_2535813
Anti-LETMD1	Sigma-Aldrich	Cat#HPA074361, RRID:AB_2686682
Anti-UCP1	Abcam	Cat#ab10983, RRID:AB_2241462
Anti-CS	Proteintech	Cat#16131-1-AP, RRID:AB_1640013
Anti-GPD2	Abcam	Cat#ab188585
Anti-SFXN5	Abcam	Cat#ab172971
Anti-TBP	Cell Signaling	Cat#44059
Anti-VCL	Sigma-Aldrich	Cat#V9264, RRID:AB_10603627
Anti-CNX	Cell Signaling	Cat#2679, RRID:AB_2228381
Bacterial and Virus Strains		
ATP1A2 overexpression adenovirus	Vector Biolabs	Cat#ADV-201680
Cre overexpression adenovirus	University of Iowa Viral Core Facility	Cat#AD5CMVCre
GFP overexpression adenovirus	University of Iowa Viral Core Facility	Cat#AD5CMVeGFP
AAV8-CMV-DIO-mATP1A2	Vector Biolabs	Custom order
AAV8-CAG-GFP-WPRE	Boston Children's Hospital Viral Core	Custom order
AAV8-U6-GFP-ATP1A2-shRNA	VectorBuilder	Custom order
AAV8-shRNA-SFXN5	VectorBuilder	Cat#VB900056-6989wbw
AAV8-shRNA-scramble	VectorBuilder	Cat# VB010000-0023jze
Biological Samples		
Chemicals, Peptides, and Recombinant Proteins		
CL316,243	Sigma-Aldrich	Cat#C5976
cOmplete™ Protease Inhibitor Cocktail	Sigma-Aldrich	Cat#CO-RO
PhosSTOP, Phosphatase Inhibitor	Sigma-Aldrich	Cat#PHOSS-RO
EPPS	Sigma-Aldrich	Cat#E9502
Bond-Breaker™ TCEP Solution, Neutral pH	ThermoFisher Scientific	Cat#77720
Iodoacetamide	Sigma-Aldrich	Cat#I1149
Dithiothreitol (DTT)	Sigma-Aldrich	Cat#DTT-RO
Lys-C	Wako Chemicals	Cat#125-05061
Trypsin	Promega	Cat#V5113
Hydroxylamine	Sigma-Aldrich	Cat#438227

REAGENT or RESOURCE	SOURCE	IDENTIFIER
Rosiglitazone	Cayman	Cat#71740
Isobutylmethylxanthine(IBMX)	Sigma-Aldrich	Cat#I7018
Dexamethasone	Sigma-Aldrich	Cat#D4902
Insulin	Sigma-Aldrich	Cat#I5500
3,3',5-Triiodo-L-thyronine (T3)	Sigma-Aldrich	Cat#T2877
Indomethacin	Sigma-Aldrich	Cat#I7378
Collagenase B	Sigma-Aldrich	Cat#COLLB-RO
Opti-MEM	ThermoFisher Scientific	Cat#31985070
Lipofectamine RNAiMAX	Invitrogen	Cat#13778-150
Thymine-d4	Cambridge Isotope	Cat#DLM-1089
Inosine-15N4	Cambridge Isotope	Cat#NLM-4264
Glycocholate-d4	Cambridge Isotope	Cat#DLM-2742
Empore SPE disk C18	VWR	Cat#76333-132
High fat rodent diet	OpenSource Diets	Cat#D12492
Formic acid	Life Technologies	Cat#85178
Norepinephrine	Sigma-Aldrich	Cat#A9512
Glycerol-3-phosphate	Sigma-Aldrich	Cat#G7886
Oligomycin	VWR	Cat#80058-538
DNP (2,4-Dinitrophenol)	Sigma-Aldrich	Cat#D198501
CCCP (carbonyl cyanide 3-chlorophenylhydrazone)	Sigma-Aldrich	Cat#C2759
Isoproterenol	Sigma-Aldrich	Cat#420355
Antimycin	Sigma-Aldrich	Cat#A8674
Rotenone	Sigma-Aldrich	Cat#R8875
Pyruvic acid	Sigma-Aldrich	Cat#107360
Malic acid	Sigma-Aldrich	Cat#M1000
GDP	Sigma-Aldrich	Cat#G7127
Sucrose	Sigma-Aldrich	Cat#S7903
BSA	Roche	Product# 3117057001
HBSS buffer	Corning	Cat#21-023-CV
Free glycerol reagent	Sigma-Aldrich	Cat#F6428
DMEM respiration medium without $NaHCO_3$	Sigma-Aldrich	Cat#D5030
TRIzol	Ambion	Cat#15596018
GoTaq qPCR master mix	Promega	Cat#A6001
Critical Commercial Assays		
High-Select Fe-NTA Phosphopeptide Enrichment Kit	ThermoFisher Scientific	Cat#A32992
Pierce™ BCA Protein Assay Kit	ThermoFisher Scientific	Cat#23225
Micro BCA™ Protein Assay Kit	ThermoFisher Scientific	Cat#23235
Qiagen RNA Mini Kit	Qiagen	Cat#12183025
Giga-MUGA genotyping assay	Neogen	Cat#550
Pierce anti-HA magnetic beads	Thermo Fisher Scientific	Cat#88836
Sep-Pak C18 Cartridges	Waters	Cat#WAT054955

REAGENT or RESOURCE	SOURCE	IDENTIFIER
Fluo-4 Calcium Imaging Kit	ThermoFischer Scientific	Cat#F10489
High-capacity cDNA reverse transcription kit	ThermoFisher Scientific	Cat#4368813
16-plex TMT reagents	ThermoFisher Scientific	Cat#A44520
TMTpro-134C&135N labeling reagents	ThermoFisher Scientific	Cat#A52046
Seahorse FluxPaks	Agilent	Part#102340
Deposited Data		
OPABAT raw files	This paper	https://www.ebi.ac.uk/pride,ID#PXD036947
OPABAT website	This paper	https://opabat.hms.harvard.edu
Experimental Models: Cell Lines		
Primary brown adipocytes	This paper	N/A
U2OS	ATCC	Cat#HTB-96
Experimental Models: Organisms/Strains		
C57BL/6J mice	The Jackson Laboratory	Cat#000664
Diversity outbred mice	The Jackson Laboratory	Cat#009376
Mito-Tagged mice	The Whitehead Institute; Bayraktar et al., 2019	N/A
LETMD^{KO} mice	This paper; Transgenic Mouse Core at Dana-Faber/HMS	N/A
Oligonucleotides		
ATP1A2 siRNA	ORIGENE	Cat#SR421739
LETMD1 siRNA	Integrated DNA Technologies	Design ID# mm.Ri.LETMD1.13
SFXN5 siRNA	Horizon Discovery	Cat#J-057802-06
sgRNA for LETMD1, AATGACGCCCCAAGAAACGA	Synthego	Custom order
Recombinant DNA		
LETMD1-HA DNA sequence	Huttlin et al., 2021	N/A
SFXN5-HA DNA sequence	Huttlin et al., 2021	N/A
Software and Algorithms		
Xcalibur	ThermoFisher Scientific	Cat#OPTON-30965
TraceFinder	ThermoFisher Scientific	Cat#OPTON-30688
Masspike (in house)	Huttlin et al., 2010	N/A
Protein Digestion Simulator	Pacific Northwest National Laboratory	https://pnnl-comp-mass-spec.github.io/Protein-Digestion-Simulator/
Comet	Eng et al., 2013	http://comet-ms.sourceforge.net
MATLAB	MathWorks	https://www.mathworks.com
R version 4.0.2	R Project	https://www.r-project.org
RStuido 2022.02.3+492	R Studio Team	https://rstudio.com
ImageJ	NIH	https://imagej.nih.gov/ij/
OME Remote Objects	Allan et al., 2012	https://www.openmicroscopy.org

REAGENT or RESOURCE	SOURCE	IDENTIFIER
Cytoscape 3.7.2	Shannon et al., 2003	https://cytoscape.org/index.html
Prism 9	GraphPad	https://www.graphpad.com/scientific-software/prism/
Pymol version 2.3.1	Schrodinger	https://pymol.org/2/
CUDA-accelerated 3D-SIM reconstruction code	Gustafsson et al., 2008	N/A
ExpeData software package	Sable Systems International	N/A
DatLab version 7.4.0.4	Oroboros Instruments	https://www.oroboros.at/index.php/product/datlab/
Other		
Q-Exactive HF-X mass spectrometer	ThermoFisher Scientific	Cat#0726042
Orbitrap Eclipse Mass Spectrometer	ThermoFisher Scientific	Cat#FSN04-10000
FAIMSPro	ThermoFisher Scientific	Cat#FMS02-10001
EASY-nLC™ 1200 System	ThermoFisher Scientific	Cat#LC140
WPS-3000TBFC Biocompatible Well Plate Autosampler	ThermoFisher Scientific	Cat#5841.0020
TCC-3000RS Thermostatted Column Compartment	ThermoFisher Scientific	Cat#5730.0000
LPG-3400RS Quaternary Pump w/Degasser	ThermoFisher Scientific	Cat#5040.0036
Multi-Therm heat-shake	Sigma-Aldrich	Cat#Z755753
Wollenberger tongs	Xiao et al., 2020	N/A
TissueLyser II	QIAGEN	Cat#85300
Luna 5 μm NH2 column	Phenomenex	Cat#00F-4378-B0
SunFire Prep C18 5 μm OBD column	Waters	Cat#186003969
2545 Binary Gradient Module	Waters	Cat#2545
2489 UV/Visible Detector	Waters	Cat#2489
High tolerance coverslips for SIM imaging	MatTek	Cat##PCS-170-1818
EchoMRI 3-in-1 body composition analyzer	Echo MRI LLC	N/A
OneTouch UltraMini blood glucose meter and test strips	LifeScan IP Holdings, LLC	N/A
Promethion indirect calorimetry system	Sable Systems International	N/A
Parr 6725EA Semimicro Calorimeter	Parr Instrument Company	Cat#6725EA
Parr 1107 Oxygen Bomb	Parr Instrument Company	Cat#1107
Oroboros O2K High-Resolution respirometer	Oroboros Instruments	Cat#10023-01
QuantStudio 6 Flex Real-Time PCR	Applied Bio-systems	Cat#4485699
Rectal temperature probe	Physitemp	Cat#RET3
Rectal temperature probe reader	Physitemp	Cat#BAT12
Seahorse XF24 Extracellular Flux Analyzer	Agilent	N/A
DeltaVision OMX Blaze	GE Healthcare	N/A